J. Fluid Mech. (2005), *vol.* 537, *pp.* 1–33.
doi:10.1017/S0022112005004684 Printed in the United Kingdom

The pulsatile motion of a semi-infinite bubble in a channel: flow fields, and transport of an inactive surface-associated contaminant

By MAXIMILLIAN E. ZIMMER IV[1], HARVEY A. R. WILLIAMS[2] AND DONALD P. GAVER III[1]†

[1]Department of Biomedical Engineering, Tulane University, New Orleans, LA 70118, USA

[2]Perforating Research, Schlumberger Reservoir Completions, 14910 Airline Rd, Rosharon, TX 77583, USA

(Received 8 July 2003 and in revised form 4 January 2005)

We investigate a theoretical model of the pulsatile motion of a contaminant-doped semi-infinite bubble in a rectangular channel. We examine the fluid mechanical behaviour of the pulsatile bubble, and its influence on the transport of a *surf*ace-*inact*ive contamin*ant* (termed *surfinactant*). This investigation is used to develop a preliminary understanding of surfactant responses during unsteady pulmonary airway reopening. Reopening is modelled as the pulsatile motion of a semi-infinite gas bubble in a horizontal channel of width $2a$ filled with a Newtonian liquid of viscosity μ and constant surface tension γ. A modified Langmuir sorption model is assumed, which allows for the creation and respreading of a surface multilayer. The bubble is forced via a time-dependent volume flux $Q(t)$ with mean and oscillatory components (Q_M and Q_ω, respectively) at frequency ω. The flow behaviour is governed by the dimensionless parameters: $Ca_M = \mu Q_M/(2a\gamma)$, a steady-state capillary number, which represents the ratio of viscous to surface tension forces; $Ca_\Omega = \mu Q_\omega/(2a\gamma)$, an oscillatory forcing magnitude; $\Omega = \omega\mu a/\gamma$, a dimensionless frequency that represents the ratio of viscous relaxation to oscillatory-forcing timescales; and $A = 2Ca_\Omega/\Omega$, a dimensionless oscillation amplitude. Our simulations indicate that contaminant deposition and retention in the bubble cap region occurs at moderate frequencies if retrograde bubble motion develops during the oscillation cycle. However, if oscillations are too rapid the ensuing large forward tip velocities cause a net loss of contaminant from the bubble tip. Determination of an optimal oscillation range may be important in reducing ventilator-induced lung injury associated with infant and adult respiratory distress syndromes by increasing surfactant transport to regions of collapsed airways.

1. Introduction

The overall goal of this study is to explore the pulsatile motion of a semi-infinite bubble in a narrow channel and its impact on the transport of soluble surface-associated contaminant. The fluid mechanical investigation is an extension of the classical steady-flow problem previously investigated by Fairbrother & Stubs (1935). Taylor (1961), Bretherton (1961) and many others. The present study may be of fundamental importance to a range of applications including the development of

† Author to whom correspondence should be addressed: donald.gaver@tulane.edu

microfluidic devices (Geng *et al.* 2001), the coating of surfaces, flow through porous media, and biological fluid mechanics (Eckmann & Diamond 2004; Ghadiali, Banks & Swarts 2002). In this paper, we investigate the general fluid flow, and the transport of a *surf*ace-*inact*ive contamin*ant* (*surfinactant*). This transport problem is investigated in order to develop a foundation for understanding transport phenomena of surface-active contaminants in this system.

Our interest in this problem stems from its relevance to pulmonary mechanics. The lung is comprised of successive generations of bifurcating airways that communicate inspired air with pulmonary alveoli for gas exchange with the blood. Distal airways are compliant structures that have a thin layer of lining fluid coating their interior surfaces. The first inspiration of a newborn clears the amniotic fluid by introducing a long bubble of air that 'opens' the airways. Healthy neonates achieve this inspiration without assistance. However, premature neonates can develop respiratory distress syndrome (RDS), where their underdeveloped lungs may have a high lining-fluid surface tension due to inadequate surfactant production. In adults, acute respiratory distress syndrome (ARDS) can result from sepsis or smoke inhalation and may also cause airway collapse. In both RDS and ARDS, treatment may require large ventilation pressures to force air into the lungs, but this is done at the risk of causing ventilator-induced lung injury (Dos Santos & Slutsky 2000; Fujiwara *et al.* 1980; Krishnan & Brower 2000; Whitehead & Slutsky 2002). Bilek, Dee & Gaver (2003) showed experimentally that mechanical stresses associated surface tension may cause epithelial cell damage, which can be prevented with a high concentration of pulmonary surfactant. This damage appears to be related to the normal-stress gradient that sweeps across the cells as the airway reopens (Kay *et al.* 2004). For more information about surfactant physicochemical hydrodynamics and pulmonary mechanical behaviour, the reader is referred to the review paper by Grotberg (2001).

RDS is treated with surfactant replacement therapy (SRT), which has been modelled by Halpern, Jensen & Grotberg (1998). The administered exogenous surfactant functions similarly to its endogenous analogue – adsorbing to the air–liquid interface, reducing the surface tension, and lowering driving pressures. Even though SRT has lowered the mortality rate, RDS remains one of the leading causes of premature infant death (MacDorman *et al.* 2002). The efficacy of SRT may be related to the delivery and transport mechanisms of the replacement surfactant. Surfactant transport is intimately connected to the fluid flow in a reopening airway. The reopening is related to two-phase flow in a flexible-walled system (Gaver *et al.* 1996; Gaver, Samsel & Solway 1990; Hazel & Heil 2003; Heil 2000; Jensen *et al.* 2002; Yap *et al.* 1994); however, many of the interfacial flow and transport properties can be understood by examining the behaviour in a rigid-walled system (Ghadiali & Gaver 2003). We will use this approximation in the present study.

When surfactant is incorporated, two major transport mechanisms must be considered: bulk convection/diffusion and interfacial sorption kinetics. Figure 1 depicts the dynamics of this surfactant transport system. The surfactant concentration of the fluid bulk, $C(\boldsymbol{x}, t)$, is in dynamic equilibrium with the subsurface concentration, $C_s(s, t)$, where s is the interfacial coordinate. Only surfactant molecules that are located in the fluid subsurface can be adsorbed to the air–liquid interface, where the surfactant concentration is denoted Γ. In the present investigation we will focus on adsorption-limited transport, which is appropriate if concentrations of surfactant are large .(Ghadiali & Gaver 2003).

Interfacial surfactant (Γ) is transported by flux to the interface and then by surface convection and diffusion. At low forward bubble velocities, fluid recirculates at the

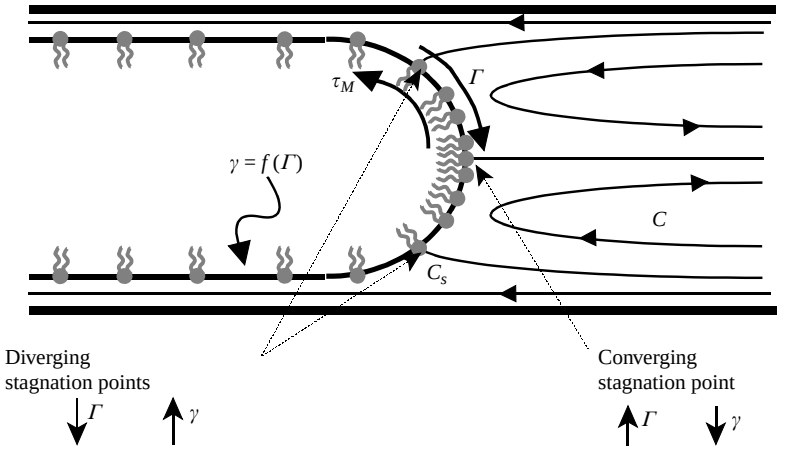

FIGURE 1. Surfactant dynamics of a Hele-Shaw cell bubble system. C designates the bulk concentration; C_s represents the subsurface fluid surfactant concentration. The surface tension γ is dependent on the local surfactant surface concentration Γ. The flow field of the system creates an uneven distribution of surfactant along the interface, which results in non-equilibrium surface tensions and Marangoni stresses τ_M, that affect the flow circulation.

bubble tip and causes convection of surfactant molecules toward the converging stagnation point at the bubble tip and away from the diverging stagnation points in the bubble transition region. We define this 'transition region' as the area of the interface connecting the uniform thin film to the bubble cap. Dynamic interfacial expansion or compression associated with bubble motion can cause the surface tension to deviate from γ_{eq}, the static equilibrium surface tension of a surfactant-doped interface. This causes both non-equilibrium normal stress and Marangoni stress, which can increase the interfacial pressure drop (Ghadiali & Gaver 2003; Ratulowski & Chang 1990; Yap & Gaver 1998). Prior studies indicate that pulmonary surfactant is not capable of adsorbing rapidly enough to eliminate non-equilibrium effects and remobilize the interface, even under extremely high concentrations. For this reason, during steady reopening the airway pressures are likely to remain large (Ghadiali & Gaver 2000).

In this paper, we investigate whether unsteady motion can be used to increase the transport of contaminant to an air–liquid interface. In particular, we explore the implications of dynamic expansion and compression of the interface and the creation of contaminant multilayers. Several studies (Diamant *et al.* 2000; Lipp *et al.* 1998; Lu *et al.* 2002; Takamoto *et al.* 2001) have shown that monolayers of pulmonary surfactant adsorbed to an air–liquid interface collapse under compression to form sub-surface multilayers (figure 2). These multilayers can respread to the primary interface when the interfacial surface area expands (Ding *et al.* 2001). Multilayer formation and respreading are key mechanisms responsible for the surface tension hysteresis observed during the cycling of a surfactant-doped air–liquid interfaces with high bulk concentrations (Krueger & Gaver 2000).

Several parameters are important when considering multilayer formation and respreading. The maximum equilibrium surface concentration, Γ_∞, represents the maximum number of molecules in sorptive equilibrium able to occupy a resting interface. The maximum dynamic surface concentration, Γ_{max}, is the maximum surface concentration of surfactant molecules the interface can withstand under area compression. At Γ_{max}, the surface monolayer will begin to collapse if compression continues.

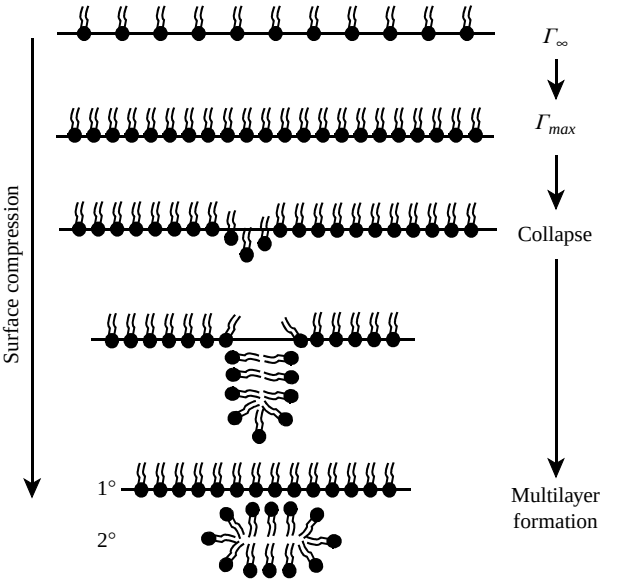

FIGURE 2. Surfactant multilayer formation under surface compression. At static equilibrium at a high bulk concentration, the primary layer (1°) surfactant concentration is Γ_∞. Under surface compression, the maximum surface concentration ($\Gamma_{\max}$) can be reached. If interface compression continues, collapse of the surfactant molecules from the interface can lead to secondary (2°) multilayer formation.

During interfacial expansion following multilayer formation, the multilayer spreading concentration, Γ_{mls}, is the minimum surface concentration that must be obtained under area expansion before respreading may occur. These critical concentrations are labelled in the surface tension–surface area hysteresis loop shown in figure 3, adapted from experimental data (Krueger & Gaver 2000).

We hypothesize that pulsatile (flow with a non-zero mean and oscillatory components) two-phase flow will create dynamic changes in the flow field that influence the transport characteristics of surfactant onto and along the bubble interface by creating cyclic interfacial expansion and contraction. In addition, this fluid flow could create and respread surfactant multilayers. In the present study, we explore the transport of a 'passive' surface-associated contaminant. While our model incorporates an energetic preference for surfinactant to be interfacially located, no surface activity is associated with this orientation. Surface transport is examined using monolayer and multilayer models assuming bulk-equilibrium dynamics characteristic of high bulk concentrations. We aim to identify a combination of pulsatile flow parameters for optimized contaminant deposition and retention in the bubble cap region. A computational model that implements a blend of boundary element method (BEM) and lubrication theory is developed to analyse this system.

2. Model formulation

We examine the pulsatile motion of a semi-infinite gas bubble in a horizontal channel of width $2a$ filled with an incompressible Newtonian liquid of viscosity μ, constant surface tension γ, and density ρ (figure 4). All flow and transport equations are expressed in the laboratory reference frame. We consider a two-dimensional Cartesian geometry with position vectors $\boldsymbol{x}^* = (x^*, y^*)$ and velocities $\boldsymbol{u}^* = (u^*(\boldsymbol{x}^*, t^*),$

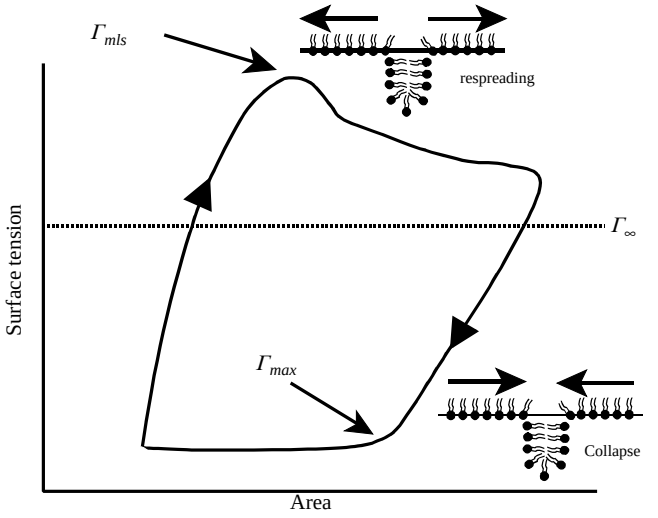

FIGURE 3. Example surface tension–area hysteresis loop from pulsating bubble surfactometer experiments using Infasurf. Surface concentrations Γ_∞, Γ_{max}, and Γ_{mls} are shown to indicate the location of collapse and respreading mechanisms in the system. Adapted from Kruegar & Gaver (2000).

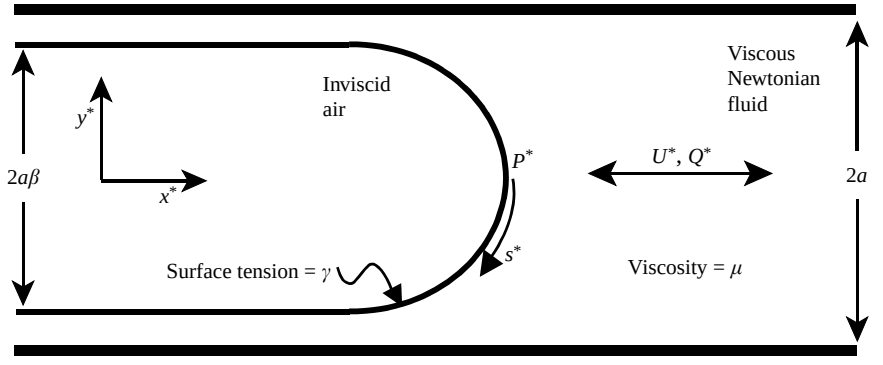

FIGURE 4. Schematic of relevant forces/parameters of the propagating bubble system.

$v^*(\boldsymbol{x}^*, t^*)$), where t^* is time, $P^* = P^*(\boldsymbol{x}^*, t^*)$ is the fluid pressure ($P^* = 0$ defines the gas-phase pressure), s^* is the distance along the meniscus from the bubble tip and the asterisk denotes dimensional variables.

A downstream two-dimensional flow rate $Q^*(t^*)$ is prescribed that, by mass conservation, determines the time-dependent behaviour of the air finger:

$$Q^*(t^*) = Q^*_M + Q^*_\omega \sin(\omega t^*), \tag{1}$$

where Q^*_M is the mean component, Q^*_ω is the oscillation amplitude component, ω is the frequency of oscillation. The resulting upstream gas finger width is $2a\beta$; the dynamics of the inviscid air is neglected.

2.1. *Governing equations*

The governing equations of fluid motion and transport are scaled to determine the dimensionless parameters describing the relative importance of various mechanisms

Timescale	Interpretation
$T_{Relax} = a\mu/\gamma$	surface-tension-driven relaxation of a viscous film
$T_{IC} = a/(Q^*/2a)$	creation of new interface of length a by the bubble lengthening with an average velocity $Q^*/2a$
$T_{Force} = 1/\omega$	rate of bubble oscillation
$(T_{Diff})_i = a^2/D_i$	surface diffusion over a length a
$T_{Ads} = 1/(k^a C_0)$	adsorption of surfinactant with a rate constant $k^a C_0$
$T_{Des} = 1/k^d$	desorption of surfinactant with a rate constant k^d

TABLE 1. Definition and description of the relevant timescales.

Dimensionless parameter	Timescale relationship
$Ca(t) = \mu Q^*(t)/(2a\gamma)$	T_{Relax}/T_{IC}
$\Omega = \omega a\mu/\gamma$	T_{Relax}/T_{Force}
$Pe_i = \gamma a/(D_i\mu)$	$(T_{Diff})_i/T_{Relax}$
$St_i^a = k_i^a C_0 a\mu/\gamma$	T_{Relax}/T_{Ads}
$St_i^d = k_i^d a\mu/\gamma$	T_{Relax}/T_{Des}
St_i^a/Ca_M	T_{IC}/T_{Ads}
St_i^d/Ca_M	T_{IC}/T_{Des}
$Pe_i \cdot Ca_M$	$(T_{Diff})_i/T_{IC}$

TABLE 2. Definition of dimensionless parameters and their relationship to timescales.

in the system using

$$\left.\begin{aligned} &\boldsymbol{u}^* = U\boldsymbol{u} = \left(\frac{\gamma}{\mu}\right)\boldsymbol{u}, \quad P^* = \left(\frac{\gamma}{a}\right)P, \quad \boldsymbol{x}^* = a\boldsymbol{x}, \quad t^* = T_{Relax}t = \left(\frac{a\mu}{\gamma}\right)t, \\ &s^* = as, \quad Q^* = \left(\frac{2\gamma a}{\mu}\right)Q, \quad h^* = ah, \quad C^* = C_0 C, \quad \Gamma^* = \Gamma_{eq}\Gamma, \\ &j^* = Jj = \left(\frac{U\Gamma_{eq}}{a}\right)j, \end{aligned}\right\} \tag{2}$$

where $h = h(x, t)$ is the height of the meniscus from the bottom wall, C_0 is the equilibrium bulk concentration, Γ_{eq} is the equilibrium surface concentration, and j^* represents the surfinactant flux magnitude. The velocity scale, $U = \gamma/\mu$, represents the interfacial relaxation velocity; thus, $T_{Relax} = a\mu/\gamma$ is the timescale related to the surface-tension-driven relaxation of a viscous film. We will see below that the relationship between T_{Relax} and other timescales for this system (interfacial creation, diffusion, and sorption, summarized in table 1) provides the basis for many of the dimensionless parameters in this model. The definitions of all dimensionless parameters are provided below, and their relationships to the timescales are summarized in table 2.

2.1.1. *Flow field*

The prescribed dimensionless volume flux and far downstream velocity profile equations are

$$\left.\begin{aligned} Ca(t) &= Ca_M + Ca_\Omega \sin(\Omega t), \\ u(y, t) &= -\tfrac{3}{2}Ca(t)(y^2 - 1), \end{aligned}\right\} \tag{3}$$

where $Ca(t) = (\mu/\gamma)(Q^*(t)/2a)$ is the capillary number with mean (Ca_M) and oscillatory (Ca_Ω) components, and $\Omega = \omega a(\mu/\gamma)$ is the dimensionless oscillation frequency.

Ca reflects not only the ratio of viscous to interfacial stresses, but also represents the ratio of two distinct timescales for this system. In this context, $Ca = T_{Relax}/T_{IC}$, where $T_{IC} = a/(Q^*/2a)$ is the timescale associated with the creation of new interface of length a by the bubble lengthening with an average velocity $Q^*/2a$. Likewise, $\Omega = T_{Relax}/T_{Force}$, where T_{Force} is the forcing timescale ($T_{Force} = 1/\omega$). The far-downstream velocity profile in (3) represents a Poiseuille flow assumption that is valid far from the bubble tip.

The oscillatory displacement amplitude $A = 2Ca_\Omega/\Omega$ represents the dimensionless stroke length of bubble oscillation. If $A = 1$, the bubble oscillates with a displacement approximately equal to the channel half-width. This parameter is used to compare effectively the system behaviour across a wide range of values for Ca_Ω and Ω in an experimentally relevant format.

We assume that inertia and unsteadiness are insignificant for the viscous flow, thus Stokes flow is appropriate:

$$\left.\begin{aligned} \nabla P &= \nabla^2 \boldsymbol{u}, \\ \nabla \cdot \boldsymbol{u} &= \boldsymbol{0}. \end{aligned}\right\} \tag{4}$$

The Stokes flow assumptions are addressed in § 5.3. It is important to note that unsteadiness still arises in the formulation from the kinematic boundary condition described below.

Fluid in contact with the channel wall satisfies no-slip and no-penetration conditions:

$$\boldsymbol{u} = 0 \text{ at } y = \pm 1. \tag{5}$$

Assuming constant surface tension, the interfacial stress jump condition is

$$[\boldsymbol{\sigma} \cdot \hat{\boldsymbol{n}}_{int}] = -\kappa \hat{\boldsymbol{n}}_{int}, \tag{6}$$

where $\boldsymbol{\sigma} = -P\boldsymbol{I} + (\nabla \boldsymbol{u} + \nabla \boldsymbol{u}^T)$ is the stress tensor for the viscous lining fluid, $\hat{\boldsymbol{n}}_{int}$ is the outward-facing interfacial normal vector, and $\kappa = \nabla \cdot \hat{\boldsymbol{n}}_{int}$ is the interfacial curvature.

We simulate this system using the boundary element method (BEM) with time-dependent boundary conditions, in accordance with the kinematic boundary condition:

$$\left.\frac{\mathrm{D}\boldsymbol{Y}}{\mathrm{D}t}\right|_{lab} = (\boldsymbol{u}_{lab} \cdot \hat{\boldsymbol{n}})\hat{\boldsymbol{n}} = (u_{lab})_n \hat{\boldsymbol{n}}, \tag{7}$$

where $\boldsymbol{Y} = \boldsymbol{Y}(x, y, t)$ is the location of points describing the interface, and $(u_{lab})_n = (\boldsymbol{u}_{lab} \cdot \hat{\boldsymbol{n}})$ is the normal component of interfacial particle velocity in the laboratory frame. The boundary element regime is coupled to a lubrication theory region that describes the thin film. This method of solution is described in § 3.

2.1.2. *Transport*

Because we model bulk-equilibrium (sorption-limited) transport in the system, the concentration of surfinactant (C^*) is assumed uniform in the fluid bulk. As we study a passive contaminant, the interfacial surface tension (γ) remains constant. We investigate both a monolayer model and a multilayer model that incorporates monolayer collapse (multilayer generation) with respreading dynamics from the secondary layer to the interfacial primary layer, following Krueger & Gaver (2000).

The governing transport equations provide solutions for $\Gamma_i(s,t)$, where $i=1,2$ for the primary (1°) and secondary (2°) layers, respectively:

$$\left.\begin{aligned} 1^\circ: \quad & \frac{\partial \Gamma_1}{\partial t} + \frac{\partial}{\partial s}(\Gamma_1 u_s) + \Gamma_1 \kappa u_n = Pe_1^{-1}\frac{\partial^2 \Gamma_1}{\partial s^2} + j_1^s - j_1^c + j_2^r, \\ 2^\circ: \quad & \frac{\partial \Gamma_2}{\partial t} + \frac{\partial}{\partial s}(\Gamma_2 u_s) + \Gamma_2 \kappa u_n = Pe_2^{-1}\frac{\partial^2 \Gamma_2}{\partial s^2} + j_2^s + j_1^c - j_2^c, -j_2^r. \end{aligned}\right\} \tag{8}$$

$Pe_i = \gamma a/D_i\mu = (T_{Diff})_i/T_{Relax}$ is the surface Péclet number, where $(T_{Diff})_i = a^2/D_i$ is the timescale for surface diffusion over a length a. D_i is the surface diffusivity for each surfinactant layer concentration, Γ_i. The velocities u_s and u_n are the interfacial tangential and normal components, respectively. The terms $(\partial/\partial s)(\Gamma u_s)$ and $\Gamma\kappa u_n$ reflect the effects due to local stretching of the interface from tangential and normal motion of a curved surface, respectively (Stone 1990). The sorption, collapse, and respreading terms are represented by the flux magnitudes j_i^s, j_i^c, and j_i^r, respectively. Far upstream we define $\partial\Gamma_i/\partial s \to 0$; however, if the domain is sufficiently long, $\Gamma_1 \to 1$, and $\Gamma_2 \to 0$. Truncation of the domain does not influence the concentration field of the bubble cap and transition regions.

The sorption flux magnitudes of the primary and secondary layers, following a modified Langmuir adsorption model, are

$$\left.\begin{aligned} 1^\circ: \quad & j_1^s = \begin{cases} (St_1^a C_s)(\tilde{\Gamma} - \Gamma_1) - St_1^d\left(\Gamma_1 - \dfrac{\Gamma_2}{2}\right), & \Gamma_1 < \tilde{\Gamma} \\ -St_1^d\left(\Gamma_1 - \dfrac{\Gamma_2}{2}\right), & \Gamma_1 \geqslant \tilde{\Gamma}, \end{cases} \\ 2^\circ: \quad & j_2^s = -St_2^d \Gamma_2, \end{aligned}\right\} \tag{9}$$

where $\tilde{\Gamma} = \Gamma_\infty/\Gamma_{eq}$ and $St_i^a = k_i^a C_0 a\mu/\gamma$ and $St_i^d = k_i^d a\mu/\gamma$ are Stanton numbers that relate T_{Relax} to the adsorption timescale ($T_{Ads} = 1/(k^a C_0)$) and desorption timescale ($T_{Des} = 1/k^d$). These sorption timescales are associated with the time required for molecular sorption to, or from, an interface with $k_i^a C_0$ and k_i^d as the adsorption and desorption rates. $\Gamma_2/2$ refers to the physical blocking of primary layer desorption that occurs if a secondary bilayer exists (figure 2) that, due to the folding geometry, only covers half of the area in comparison to the same concentration on the 1° layer.

The collapse and respreading flux magnitudes are

$$j_1^c = -\Gamma_1 \kappa u_n - \frac{\partial}{\partial s}(\Gamma_1 u_s), \qquad \Gamma_1 \geqslant (\tilde{\Gamma}_{max})_1, \tag{10}$$

$$j_2^c = -\Gamma_2 \kappa u_n - \frac{\partial}{\partial s}(\Gamma_2 u_s), \qquad \Gamma_2 \geqslant (\tilde{\Gamma}_{max})_2, \tag{11}$$

$$j_2^r = \Gamma_2 \kappa u_n + \frac{\partial}{\partial s}(\Gamma_2 u_s), \qquad \Gamma_1 \leqslant \tilde{\Gamma}_{mls}, \tag{12}$$

where $(\tilde{\Gamma}_{max})_1 = (\Gamma_{max})_1/\Gamma_{eq}$, $(\tilde{\Gamma}_{max})_2 = 2(\tilde{\Gamma}_{max})_1$, and $\tilde{\Gamma}_{mls} = \Gamma_{mls}/\Gamma_{eq}$. These fluxes reflect the transfer of surfinactant between the 1° and 2° layers that must occur due to surface stretching dynamics. Equation (10) allows the surfinactant to maintain a constant 1° layer concentration as the interface is compressed to concentrations greater than $(\tilde{\Gamma}_{max})_1$ by balancing the surface stretching terms in (8). Upon expansion (12) reintroduces surfinactant from the 2° layer to the 1° layer if surfinactant concentration

in the 1° layer falls below $\tilde{\Gamma}_{mls}$. Here, collapse from the 1° layer to the 2° layer can only occur once the 1° layer has reached the maximum allowable interfacial concentration, $(\tilde{\Gamma}_{max})_1$. Respreading from the 2° layer back to the 1° layer can occur only under conditions of interface expansion (i.e. $(\kappa u_n + \partial u_s/\partial s \geqslant 0)$ once the 1° layer concentration has decreased below the critical multilayer respreading concentration, $\tilde{\Gamma}_{mls}$. We define $(\tilde{\Gamma}_{max})_2 = 2(\tilde{\Gamma}_{max})_1$ to account for the folding of the 1° layer into the bilayer that forms the 2° layer (figure 2).

2.2. *Parameter values*

Our goal is to investigate the relationship between surfinactant adsorption to an air–liquid interface that is dynamically changing its length. If the timescales for surfinactant sorption (T_{Ads} and T_{Des}) are less than the timescale for interfacial growth (T_{IC}), the surface concentration will remain in near equilibrium. As we shall see, these timescales are not equivalent for pulmonary surfactant, and we set our transport parameters accordingly to investigate this situation.

We assume values for the system properties that reflect a two-dimensional representation of a bronchial airway ($\mu = 0.05\,\mathrm{g\,cm^{-1}\,s^{-1}}$, $\gamma_{eq} = 25\,\mathrm{dyn\,cm^{-1}}$, $a = 0.1\,\mathrm{cm}$, $Q_M = 0.1\,\mathrm{cm^2\,s^{-1}}$, $k^a \sim 0.5\,\mathrm{cm^3\,mg^{-1}\,s^{-1}}$, $C_0 = 1\,\mathrm{mg\,ml^{-1}}$) following Ghadiali & Gaver (2000). These estimates provide $Ca_M = T_{Relax}/T_{IC} \sim 10^{-3}$ and $St_i^a = T_{Relax}/T_{Ads} \sim 10^{-4}$, where *IC* denotes Interface Creation. Most importantly, $T_{IC}/T_{Ads} = St_i^a/Ca_M \sim 10^{-1}$, so the adsorption timescale is much greater than T_{IC}. Thus, adsorption will not be rapid enough to create an equilibrium surface concentration at the growing interface.

Unfortunately, simulating the dynamic system at $Ca \sim O(10^{-3})$ is not feasible because of the creation of very thin films that are difficult to resolve with the boundary element method. Thus, we increased Ca_M to $O(10^{-1})$, which still produces a thin film and maintains $T_{Relax} < T_{IC}$. To maintain the correct transport balances, sorption parameters must be adjusted in accordance with the increased Ca_M so that $T_{IC}/T_{Ads} = St_i^a/Ca_M \sim 10^{-1}$. This implies that adsorption is ten times slower than the creation of new interface. For this reason, for $Ca_M = 10^{-1}$ we study $St_i^a = 10^{-2}$. Similarly, $St_i^d/Ca_M = 10^{-3}$ is investigated by letting $St_i^d = 10^{-4}$. This maintains the correct ratio of desorption to interface creation, and ensures that the desorption rates are two orders of magnitude less than adsorption rates.

Physiologically, the surface Péclet number is approximately $Pe_i = T_{Diff}/T_{Relax} \sim 5 \times 10^7$. To preserve the relationship between surface diffusion and interfacial creation, $Pe_i Ca_M = T_{Diff}/T_{IC} \sim 5 \times 10^4$. This implies that the creation of new interface is much faster than the interfacial diffusion of surfinactant. We preserve the small diffusive effects characteristic of the physiologic system while using a smaller, more computationally stable, Péclet number by maintaining $(Pe_i Ca_M) = 50$. Calculations on a subset of problems at $Pe\,Ca = 100$ indicated that the behaviour of the system was insensitive to an increase in $Pe_i Ca_M$; in all cases diffusion was sufficiently small that its primary function was to provide numerical stability. This indicates that $Pe_i Ca_M = 50$ was adequate to determine the behaviour of the system.

We investigate the dimensionless frequency, $\Omega = T_{Relax}/T_{Forcing} = \mu\omega a/\gamma$ over the range $0.005 \leqslant \Omega \leqslant 5$, in search of optimal transport behaviour. To investigate the response in detail, we focus on three frequencies: low ($\Omega = 0.025$), moderate ($\Omega = 0.085$), and high ($\Omega = 0.4$) for $Ca_M = 0.1$, $A = 5$. These values of Ω span quasi-steady to highly unsteady responses. Furthermore, these studies permit us to explore the general characteristics of the transport behaviour and identify features that result in optimal surfinactant uptake, which occurs near $\Omega = 0.085$.

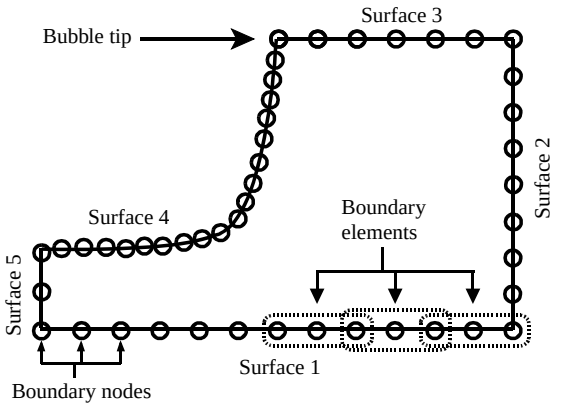

FIGURE 5. Node discretization of boundary element method region. A higher density of nodes along the interface is necessary for precise calculation of curvature and normal stress.

Surface	u	v	τ_x	τ_y
1	0	0	–	–
2	$(-3/2)Ca(t)(y^2-1)$	0	–	–
3	–	0	0	–
4	–	–	$\kappa\hat{\boldsymbol{n}}_x$	$\kappa\hat{\boldsymbol{n}}_y$
5	$-\frac{1}{2}\kappa_{x_{end}}[(y+1)^2-2(h+1)(y+1)]$	–	–	$\kappa_{x_{end}}[(y+1)-(h+1)]$

TABLE 3. Dimensionless boundary conditions used on the surfaces in the boundary element method regime specified in figure 5. $\kappa_{x_{end}}$ represents $\partial\kappa/\partial x$ at the junction between the boundary element and lubrication theory regimes.

3. Method of solution

3.1. *Boundary element method (BEM)*

Symmetry along the channel centreline allows the half-domain of the bubble tip region to be discretized into a series of quadratic elements along each of five surfaces as shown in figure 5. At each BEM node, four flow quantities describe the complete solution: the velocities u and v, as well as τ_1 and τ_2, the x and y stresses. One value of stress or velocity for each direction must be specified in the problem formulation; the system is solved for the remaining quantities in accordance with the Stokes equations using the BEM formulation described in Halpern & Gaver (1994) and Pozrikidis (1992). A complete listing of the velocity and stress quantities stipulated for each surface of the boundary is given in table 3. Conditions must be carefully specified at the corners of the domain to account for discontinuous boundary conditions (table 4).

3.2. *Lubrication theory*

To shorten the boundary element region and identify suitable boundary conditions for the BEM domain, lubrication theory was used to describe the thin liquid film dynamics along the channel wall upstream of the bubble tip. Following standard lubrication theory approximations, we define the position of the air–liquid interface at $y = h(x, t)$, and the evolution equation for this region in the inertial frame of reference is

$$\left.\frac{\partial h}{\partial t}\right|_{lab} = \frac{1}{3}\frac{\partial}{\partial x}\left(h^3\frac{\partial \kappa}{\partial x}\right). \tag{13}$$

Position	(x, y)	u	v	τ_x	τ_y
First node on S1	$(-3, -1)$	–	0	$\kappa_{x_{end}}(h)$	–
Last node on S1	$(3, -1)$	–	0	$-3Ca(t)$	–
First node on S2	$(3, -1)$	–	0	–	$3Ca(t)$
Last node on S2	$(3, 0)$	$(3/2)Ca(t)$	–	–	0
First node on S3	$(3, 0)$	–	0	0	–
Last node on S3	$(0, 0)$	–	0	0	–
First node on S4	$(0, 0)$	–	–	$-\kappa_{tip}$	0
Last node on S4	$(-3, \mathrm{h})$	–	–	$\kappa_{end}\hat{\boldsymbol{n}}_{4_x}$	$\kappa_{end}\hat{\boldsymbol{n}}_{4_y}$
First node on S5	$(-3, \mathrm{h})$	–	–	$-\kappa_{end}$	0
Last node on S5	$(-3, -1)$	0	–	–	$-\kappa_{end}(h)$

TABLE 4. Dimensionless corner conditions (rotating counterclockwise around the domain) specified for BEM domain. n_x and n_y are the x- and y-components of the normal vector, respectively.

Far upstream we impose $\mathrm{d}h/\mathrm{d}x = 0$ so that the thin film remains quiescent. Note that we have retained the full curvature terms in this version of the lubrication theory, instead of representing $\kappa \sim \partial^2 h/\partial x^2$. These terms were retained because κ is fundamental to the application of the BEM, and were available because of our use of a master surface that connected the lubrication and BEM domains (see § 3.4).

3.3. *Kinematic translation to the meniscus frame of reference*

To prevent elongation of the computational domain throughout the simulation, we translate the node-points using a reference frame that is fixed to the bubble tip (*meniscus frame*). It is important to note that this translation is performed kinematically and does not affect the equations of motion, which are based in the inertial (*laboratory*) frame of reference. The translation is achieved by subtracting the tip velocity, u_{tip}, from the x-component of velocity calculated from the equations of motion. In the meniscus frame, the bubble tip is thus always located at $(0, 0)$ on the (x, y) spatial coordinate axes.

In the boundary element region, the nodes are moved only in the direction normal to the interface, which maintains the nodal spacing more effectively than if they were allowed to move tangentially. In the meniscus frame, the interfacial evolution equation (7) becomes

$$\left.\frac{\mathrm{D}\boldsymbol{Y}}{\mathrm{D}t}\right|_{men} = [(u_{lab})_n - u_{tip}n_x]\hat{\boldsymbol{n}}, \tag{14}$$

where n_x is the x-component of the surface normal unit vector, and $(u_{lab})_n = (\boldsymbol{u}_{lab} \cdot \hat{\boldsymbol{n}})$. In the meniscus frame for the lubrication domain, the laboratory frame kinematic boundary condition (13), responsible for nodal displacement becomes

$$\left.\frac{\partial h}{\partial t}\right|_{men} = \frac{1}{3}\frac{\partial}{\partial x}(h^3\kappa_x) - u_{tip}n_x. \tag{15}$$

3.4. *Time stepping*

A critical feature that was necessary to achieve a converged solution was the accurate geometrical definition of interfacial normal unit vectors and curvatures. For this, we used a single master interface that spans the boundary element (BEM) and lubrication theory (LUB) domains. Nodal velocities in the lubrication domain are calculated using cubic splines of the interfacial shape h to determine interfacial values for use in (15).

With the boundary and corner conditions defined following tables 3 and 4, the BEM equations were solved to compute the unknown interfacial velocities in the bubble cap region. The LUB and BEM data were combined with the interfacial geometrical characteristics to quantify the rates of change of the 1° and 2° layer concentrations in accordance with the transport equations (8). Simultaneous time stepping of the flow-field and transport equations was accomplished using the NetLib subroutine LSODES (Livermore Solver for Ordinary Differential Equations with general Sparse Jacobain matrices). After each 10th cycle, the nodal positions were redistributed, and the next cycle restarted with the new definitions of interfacial geometry.

The time-stepping process was repeated until a converged cycle (termed *stationary state*) was achieved, where the tip-frame nodal positions and the interfacial concentrations did not change significantly from cycle to cycle. We used 2-norms to evaluate the change between successive cycles. For concentration, we defined

$$\|\Gamma\|_2 = \frac{1}{N}\sqrt{\sum_{i=1}^{N}(\Gamma_{i,t} - \Gamma_{i,t-T})^2},$$

where N equals the number of points in the boundary element regime. To compare convergence between systems of different frequencies, our convergence criterion was based upon $\|\Gamma\|_2/(\text{unit dimensionless time}) = \Omega\|\Gamma\|_2$. We deemed a solution as converged when $\Omega\|\Gamma\|_2 < 5\times10^{-4}$. Decreasing this convergence criterion did not modify our results (less than 0.1 % variation in results at stationary state). Parameters were varied sequentially, using the last converged solution as the initial condition for the subsequent parameter set.

4. Results

In this section we discuss first the flow field for steady and pulsatile flow to provide a qualitative description of the fluid flow that influence the transport phenomena. Second, the nature of these steady and pulsatile flow fields is related to the instantaneous interfacial concentration responses. Finally, cycle and cycle-spatial averaging techniques are used to evaluate the average response to pulsatile forcing for a single combination of Ca_M and A over a range of Ω. Although we performed analyses for all combinations of $Ca_M = 0.1$, 0.05 and $A = 1$, 5, we present detailed data only for $Ca_M = 0.1$ and $A = 5$. Cycle-averaged data are shown for other combinations of parameter values. Since the system is symmetric with respect to the channel centreline, half-domain data are presented for all flow-field representations. As stated above, we span values of Ω to determine optimal responses, and investigate the behaviour in detail for three values of Ω: low ($\Omega = 0.025$), moderate ($\Omega = 0.085$) and high ($\Omega = 0.4$). The moderate value of Ω provides nearly optimal transport for $Ca_M = 0.1$, $A = 5$, and the optimization of this transport will be explored in detail.

4.1. *Flow field*

Figure 6(*a*) presents the streamlines for steady forward flow with $Ca_M = 0.1$. In the general case of forward steady-state motion, the flow field is characterized by two stagnation points: a converging (+) stagnation point located at the bubble tip and a diverging (−) stagnation point located along the interface toward the thin-film region. In the meniscus frame, fluid is driven along the interface away from the diverging transition-region stagnation point toward the thin film and the bubble tip. In § 5, we refer to this flow type as 'Case I'.

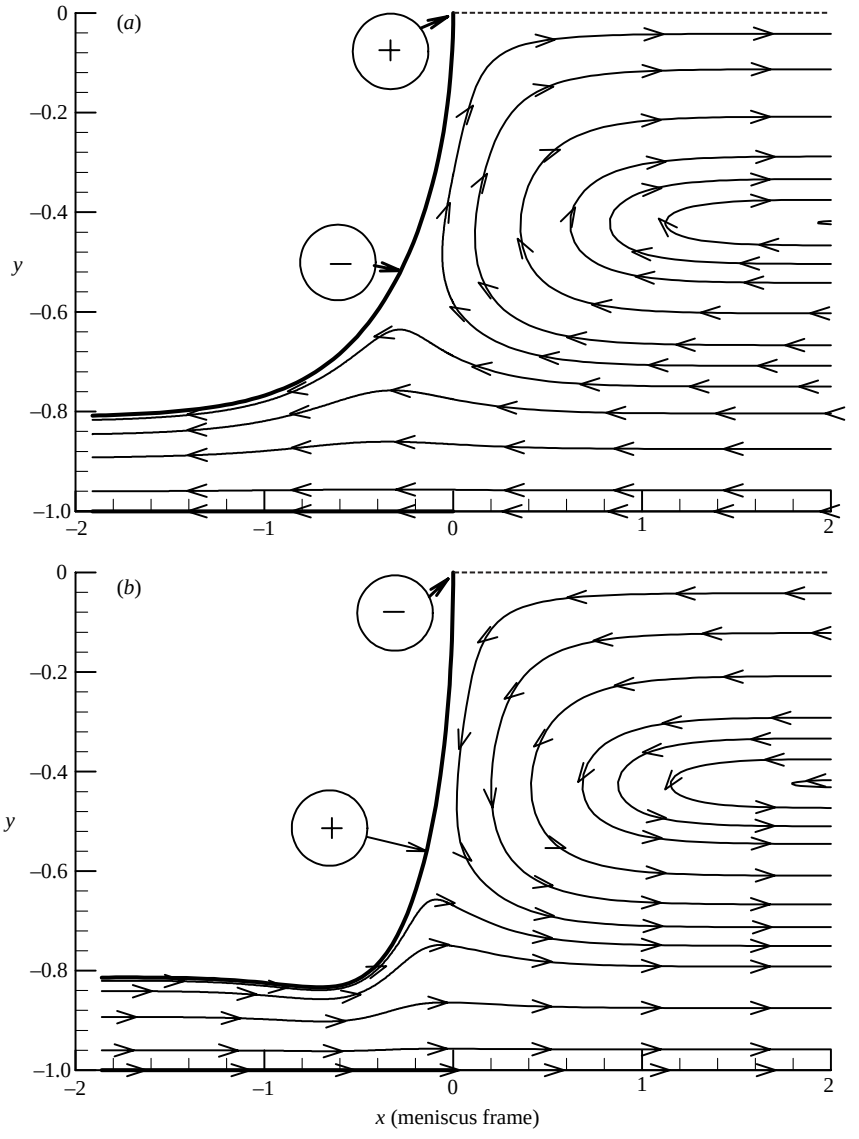

FIGURE 6. Forward (*a*) and reverse (*b*) steady-state flow streamlines. The location of the converging (+) and diverging (−) stagnation points at the tip and in the interfacial transition region are shown for $Ca_M = \pm 0.1$.

Streamlines for steady reverse flow with $Ca_M = -0.1$ are presented in figure 6(*b*). Here, the flow field is also characterized by two stagnation points: a diverging (−) tip stagnation point and a converging (+) transition-region stagnation point. In the meniscus frame, fluid is driven along the interface from both the tip and the thin film toward the transition region. This type of flow will later be referred to as 'Case III' in § 5.

Throughout the pulsatile motion, the instantaneous locations of the converging and diverging stagnation points along the meniscus are important in determining the interfacial transport dynamics of the system. Figure 7 shows the instantaneous streamlines for $Ca_M = 0.1$, $A = 5$, and $\Omega = 0.085$, with plots (*a–f*) evenly spaced every

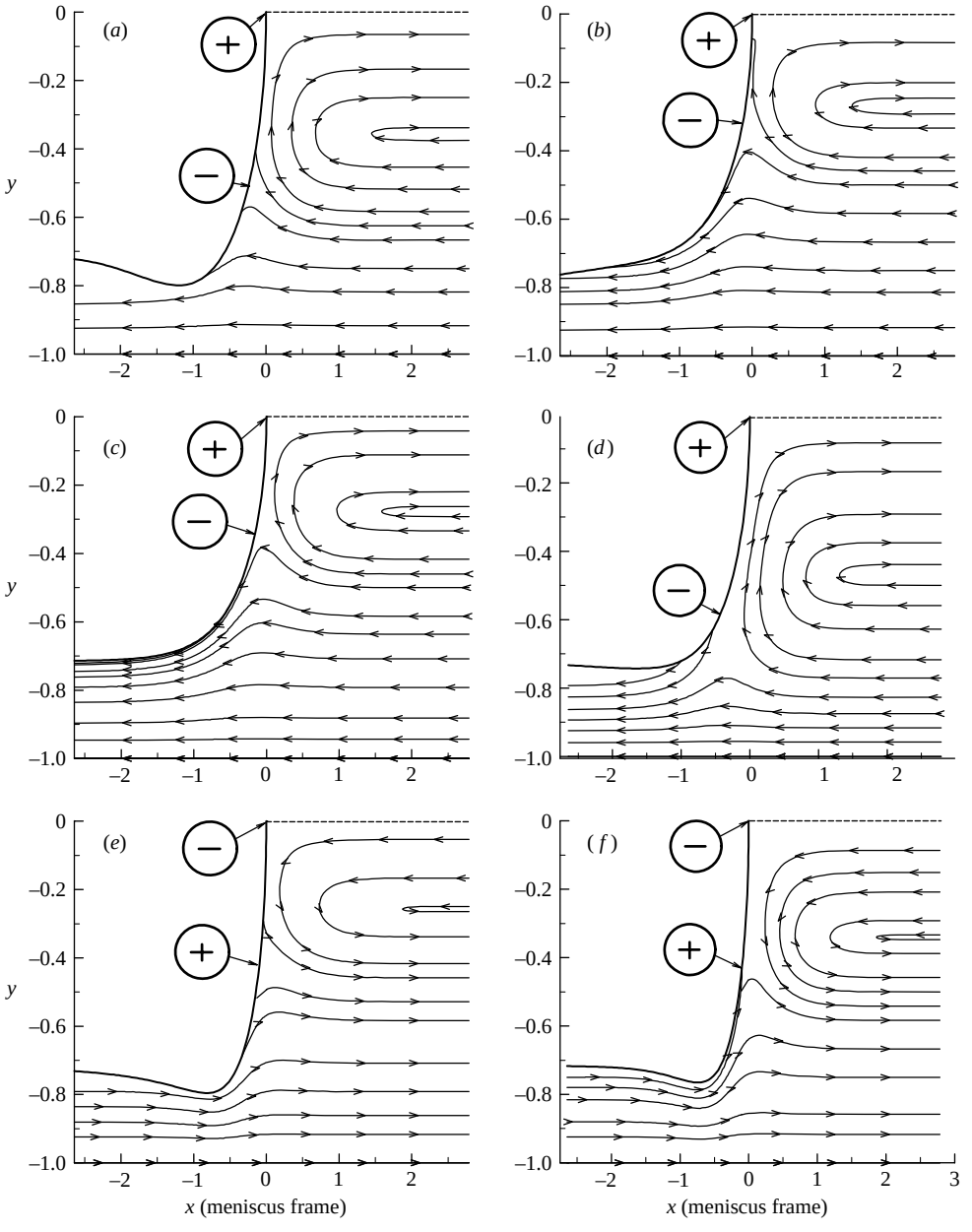

FIGURE 7. Instantaneous streamlines for points every 1/6 cycle for $Ca_M = 0.1$, $A = 5$, $\Omega = 0.085$. Note that the tip stagnation point is converging (+) in frames (*a–d*) and diverging (−) in frames (*e*, *f*). Conversely, the transition-region stagnation point switches from diverging (*a–d*) to converging (*e*, *f*).

sixth of the cycle. Note that since this is an unsteady system, the interface is not a streamline, and thus streamlines can intersect the interface. Converging tip and diverging transition-region stagnation points exist for points (*a–d*). For each of these instances, though, the diverging stagnation point is at a different location along the meniscus, changing the length of interface characterized by tip-directed fluid sweeping.

At points (*e*) and (*f*), diverging tip and converging transition-region stagnation points are evident. Again, the location of the converging stagnation point is different for the two cycle points. Figure 7 also demonstrates the variation in film thickness that occurs throughout an oscillation cycle.

Figure 8 shows the relationship between the bubble velocity (u_{tip}), tip curvature (κ_{tip}) and tip pressure drop (ΔP_{tip}) as a function of the applied $Ca(t)$ for $Ca_M = 0.1$ and $A = 5$ for $\Omega = 0.025$, 0.085 and 0.4. Figure 8(*a*) shows only small hysteresis areas for u_{tip} for each Ω, with u_{tip} at $Ca(t) = Ca_M$ nearly identical to the steady-state value (shown by the ●). However, as demonstrated below, the cycle-averaged velocity is increased by oscillation, which has an impact on the fluid volume that coats the channel wall. In contrast, κ_{tip} (figure 8*b*) demonstrates clear hysteresis that increases in magnitude with increasing Ω. The counterclockwise direction for these loops shows that as the bubble tip is accelerating, the curvature is smaller than it is in the deceleration phase. In addition, κ_{tip} at $Ca(t) = Ca_M$ differs significantly from the stationary-state value during both the accelerating and decelerating phases. At high oscillation rates ($\Omega = 0.4$), the curvature becomes negative during reverse flow, as demonstrated by the meniscus profile shown in the inset of figure 8(*b*). This results in a temporary tip-splitting response that disappears during the forward phase of the oscillation. Figure 8(*c*) shows that the time-dependent ΔP_{tip} has hysteresis that increases with increasing Ω. In addition, the slope of this hysteresis loop ($\mathrm{d}(\Delta P_{tip})/\mathrm{d}(Ca)$) increases at moderate frequencies ($\Omega = 0.085$); however, the low- and high-frequency oscillations result in equivalent slopes. Note that the direction of rotation of the ΔP_{tip} loop is the same as the κ_{tip} loop, indicating that the curvature dictates much of the pressure-drop characteristic. However, for moderate oscillation ($\Omega = 0.085$) $\Delta P_{tip} < 0$ during reverse flow even though $\kappa_{tip} > 0$; this is an indication of the importance of viscous stresses in determining the interfacial pressure drop during oscillation.

Figure 9 and figure 10 present the average interfacial and flow characteristics that are modified by the introduction of an oscillatory component to the steady flow. Figure 9(*a*) shows that the cycle-averaged tip velocity ($\bar{u}_{tip}$) increases with pulsatility. A marked increase in $\bar{u}_{tip}$ compared to the steady-state value occurs at larger Ω when Ca_M is increased; however, this transition is not coincident with the onset of retrograde motion ($Ca_\Omega = Ca_M$). An increase in oscillation magnitude from $A = 1$ to $A = 5$ causes an increase of $\bar{u}_{tip}$, with approximately a 15 % gain occurring with high-magnitude oscillation.

Figure 9(*b*) shows the average tip curvature ($\bar{\kappa}_{tip}$) as a function Ω. Here, the behaviour is clearly non-monotonic. With $A = 1$, $\bar{\kappa}_{tip}$ increases until $\Omega \sim 1$; subsequently $\bar{\kappa}_{tip}$ decreases dramatically for larger values of Ω. Since $Ca_\Omega = A\Omega/2$, the initial increase in curvature is consistent with the Ca-dependent increase in curvature that occurs during steady flow. The subsequent reduction in $\bar{\kappa}_{tip}$ occurs at large Ω, indicating that unsteadiness is responsible for the reduction. In contrast, the $A = 5$ simulations demonstrate a decrease in $\bar{\kappa}_{tip}$ at low Ω, but then show an increase in $\bar{\kappa}_{tip}$ over approximately $0.05 < \Omega < 0.2$. For larger values of Ω the curvature again decreases. The reduction in the average curvature at large Ω is a direct result of the negative curvature that occurs during the reverse flow, demonstrated in figure 8(*b*).

Figure 9(*c*) demonstrates the average ΔP_{tip} ($\overline{\Delta P}_{tip}$) vs. Ω. For $A = 1$, $\overline{\Delta P}_{tip}$ increases monotonically. In contrast, for $A = 5$ $\overline{\Delta P}_{tip}$ demonstrates a slight reduction to a minimum pressure drop that is nearly coincident with the minimum κ_{tip}. With increasing Ω, $\overline{\Delta P}_{tip}$ grows monotonically. Since this increase occurs over a range where κ_{tip} has a local maximum, viscous contributions must be responsible for the increase in $\overline{\Delta P}_{tip}$ at large Ω.

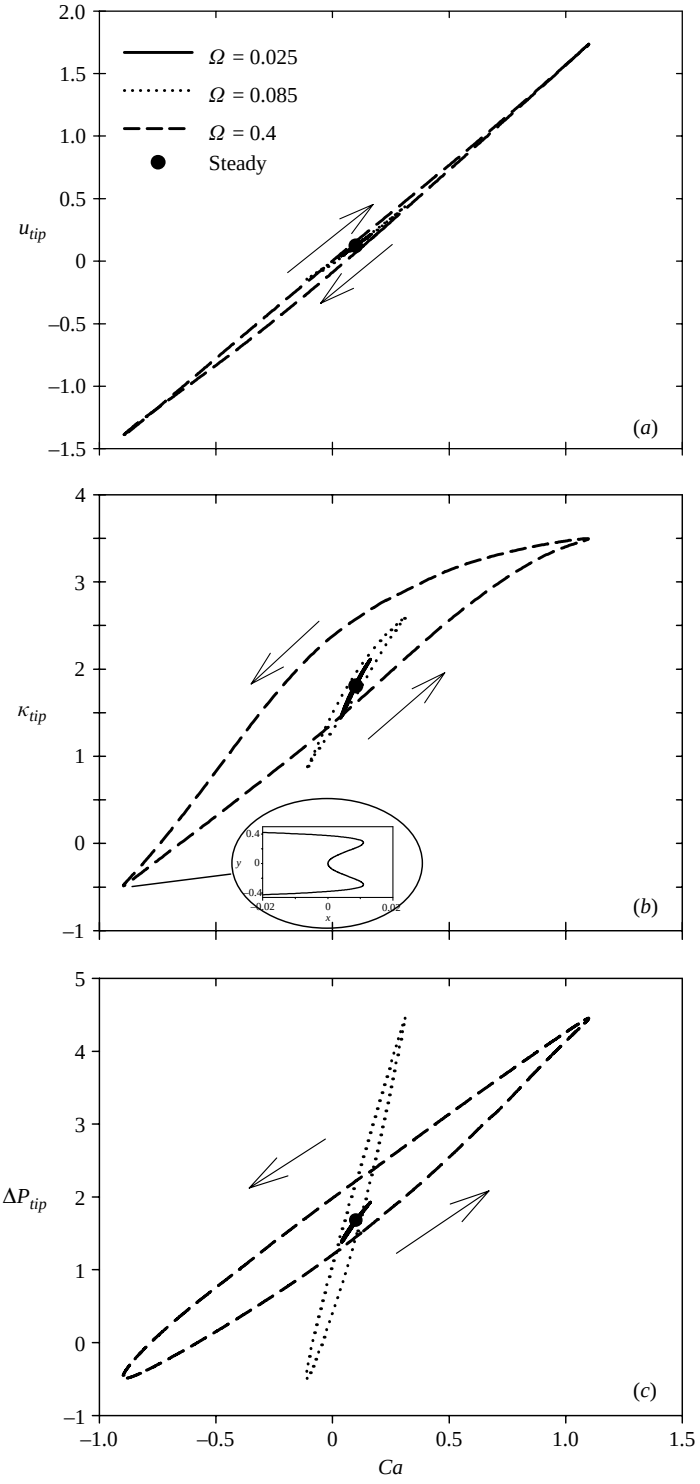

FIGURE 8. Stationary-state relationship between (*a*) the time-dependent velocity, (*b*) tip curvature and (*c*) ΔP_{tip} *vs. Ca* for $Ca_M = 0.1$, $A = 5$ and $\Omega = 0.025$ (—), $\Omega = 0.085$ (· · · · · ·) and $\Omega = 0.4$ (- - - -). ● shows steady state, $Ca_M = 0.1$. Inset of (*b*) shows the negative κ_{tip} that occurs during reverse flow of high-frequency, high-amplitude oscillation.

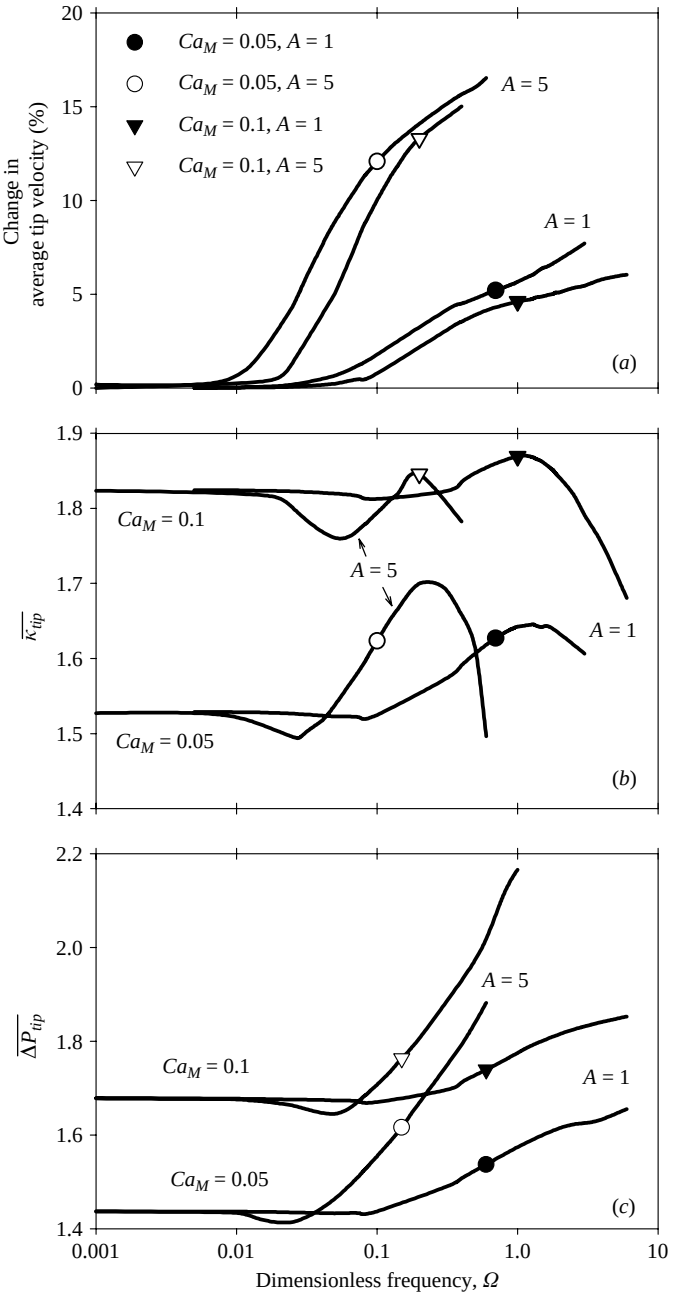

FIGURE 9. The effect of oscillation on (*a*) the average bubble velocity, (*b*) average tip curvature and (*c*) average tip pressure drop. The percentage change in velocity is calculated as the change in the cycle-averaged tip velocity with respect to the tip velocity for the steady case ($\Omega = 0$).

Figure 10 shows the modification of the far-upstream dimensionless bubble width, $\bar{\beta} = \bar{\beta}^*/a$, that is predicted in the constant-amplitude pulsatile system over a range of Ca_Ω; $\bar{\beta}$ was determined from mass conservation on a control volume surrounding the bubble tip, which shows that $\bar{\beta} = Ca_M/\bar{u}_{tip}$. The monotonic decrease in the bubble

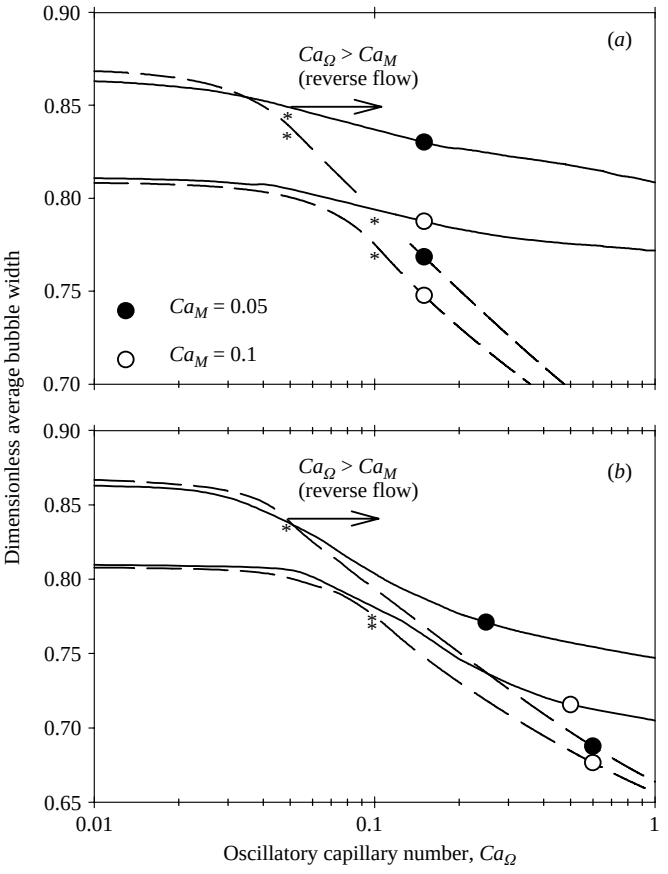

FIGURE 10. Average dimensionless bubble width. (*a*) $A = 1$, (*b*) $A = 5$. —, BEM predictions; – – – quasi-steady approximations. Note the thickening of the residual film as Ca_Ω is increased. * indicates $Ca_\Omega = Ca_M$; $Ca_\Omega > Ca_M$ results in reverse flow over a portion of the oscillation.

width is thus related directly to the monotonic increase in the average tip velocity shown in figure 9(*a*). A quasi-steady prediction of $\bar{\beta}$ is shown by the dashed lines in figure 10. By conservation of mass,

$$\bar{\beta} = \frac{\displaystyle\int_0^T \beta u_{tip}\,\mathrm{d}t}{\displaystyle\int_0^T u_{tip}\,\mathrm{d}t} \tag{27}$$

where $u_{tip} = Ca/\beta(Ca)$, $\beta(Ca)$ is the steady-state bubble width prediction from Halpern & Gaver (1994), $T = 2\pi/\Omega$ is the oscillation period, and $Ca(t)$ is given by equation (3).

The calculation of a quasi-steady approximation of $\bar{\beta}$ from (16) requires an approximation of the bubble width during bubble retraction ($Ca(t) < 0$). Two alternatives were investigated:

(i) the bubble width during retraction is approximated as equal to the average bubble width during forward bubble motion;

(ii) the bubble width during retraction is approximated as equal to the bubble width that existed during the forward phase at any given physical location.

The results of these models deviate from each other by less than 1 % over the range of parameters we investigated, so method (i) is used for the quasi-steady approximations given below.

The quasi-steady approximations are in good agreement with the BEM calculations up to $Ca_\Omega \sim Ca_M$; this range is extended with increasing A to include regions where bubble retraction occurs ($Ca_\Omega > Ca_M$). This provides an estimate for the range of $\Omega = 2Ca_\Omega/A$ that can be predicted using quasi-steady analysis, and indicates that for large A the average behaviour is faithfully captured using estimates from constant forward-flow calculations, even though the unsteady problem includes bubble retraction.

The predictions of bubble narrowing provided in figure 10 indicate that increasing the frequency of oscillation will deposit a more voluminous film on the airway wall. By increasing the film volume, the quantity of soluble surfactant contained within the film would be commensurately increased. This film thickening could provide a reservoir of surfactant that can be adsorbed to the air–liquid interface in cases of diffusion limitation that can occur at low concentrations (Ghadiali & Gaver 2003).

4.2. *Steady-state and instantaneous interfacial concentrations*

Here we show the influence of the flow fields described above on the interfacial concentration fields. In the descriptions below, the term 'buildup' indicates the relative increase in the local concentration due to converging flow. When the concentration exceeds $\Gamma_{max} = 1.3$, surfinactant is rejected from the 1° layer. Alternatively, 'depletion' refers to the relative decrease of concentration due to diverging flow. The steady-state forward-flow interfacial concentration profile for $Ca_M = 0.1$ (figure 11*a*) shows a buildup at the bubble tip and a depletion in the transition region caused by the sweeping of fluid toward the bubble tip and the thin film from the transition region. Concentration profiles for the monolayer model and the 1° and 2° layers of the multilayer model are shown. At the bubble tip, the 1° layer concentration is limited by the maximum concentration ($\Gamma_{max} = 1.3$), with excess surfinactant collapsing from the interface. Both monolayer and multilayer models demonstrate tip concentrations that reflect rejection from the 1° interface layer. In the multilayer model case, this rejection forms the 2° layer that, in turn, reduces desorption from the 1° layer. This inhibition increases the concentration of the 1° layer over that seen from the monolayer case.

Steady reverse-flow concentration profiles are given in figure 11(*b*) for $Ca_M = -0.1$. The same principles discussed for surface transport in forward steady flow hold for transport conditions characteristic of backward motion. Figure 11(*b*) shows buildup in the transition region and depletion at the tip for both monolayer and multilayer simulations. Both models show transition-region rejection from the 1° interface layer either to the bulk (monolayer model) or to the 2° layer (multilayer model).

For the pulsatile investigations, we evaluate the constant-amplitude behaviour of the system. As such, Ω and Ca_Ω are varied in concert to maintain a consistent stroke length ($A = 2Ca_\Omega/\Omega$) over a wide range of oscillation frequencies. Figure 12 shows the instantaneous capillary number for low ($\Omega = 0.025$), moderate ($\Omega = 0.085$), and high ($\Omega = 0.4$) frequencies versus t for $Ca_M = 0.1$, $A = 5$. Reverse flow only occurs in cases where $Ca_\Omega = A\Omega/2 > Ca_M$.

Figure 13 depicts the monolayer model Γ versus interfacial position (s) at evaluation points (a–f) corresponding to every 1/6 cycle for low ($\Omega = 0.025$), moderate

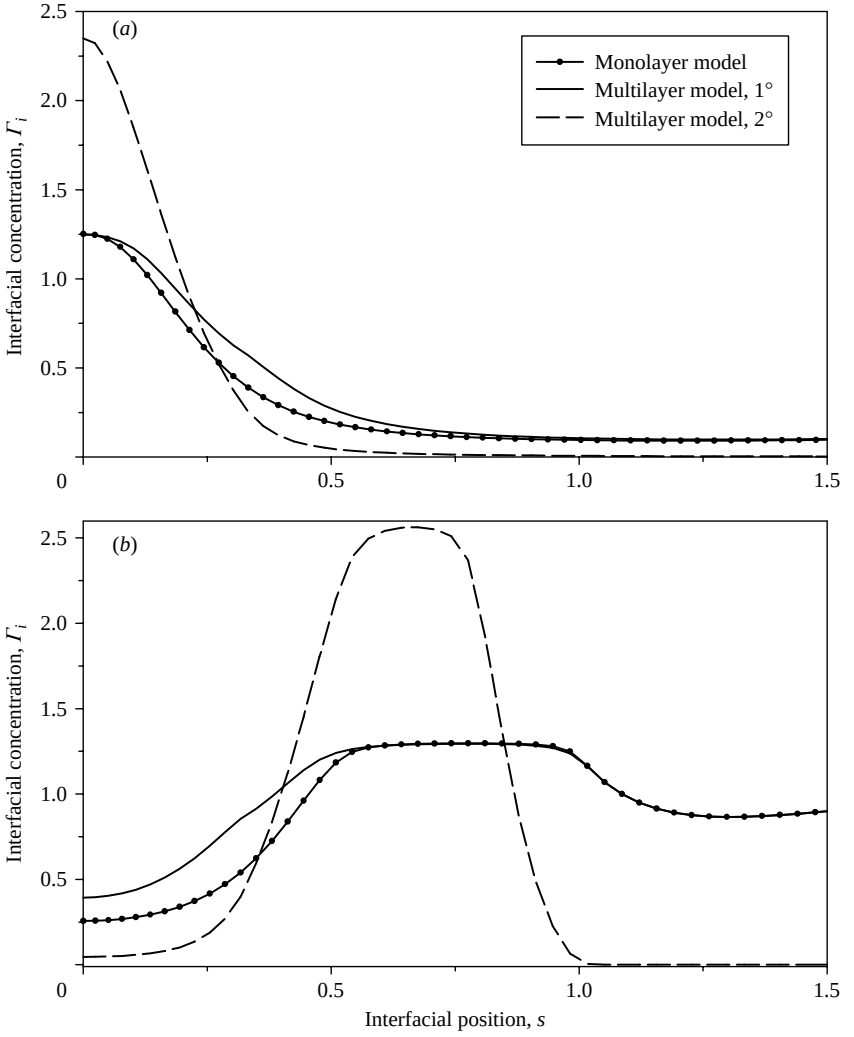

FIGURE 11. Monolayer-model *vs.* multilayer-model steady-state interfacial surfinactant concentration profiles for (*a*) forward and (*b*) reverse flow with $Ca_M = \pm 0.1$.

($\Omega = 0.085$), and high ($\Omega = 0.4$) frequencies for $Ca_M = 0.1$, $A = 5$. Note that all low frequency ($\Omega = 0.025$) profiles have a characteristic tip concentration buildup and corresponding depletion in the bubble transition region ($s \sim 0.5$) similar to the forward steady-state case (figure 11*a*). This quasi-steady behaviour occurs because $Ca_\Omega = A\Omega/2$, and thus the variation in Ca is very small. High frequency ($\Omega = 0.4$) behaviour is notably different – retrograde motion portions of the cycle (profiles *e* and *f*) show buildup in the transition region and depletion at the bubble tip similar to that of steady backward flow (figure 11*b*). However, this buildup is not maintained during the forward flow phases of the cycle, as evidenced by the low tip and transition-region concentrations seen in profiles (*b*) and (*c*). Profiles (*a*) and (*d*) represent transition states between the characteristic forward and reverse flow behaviour portions of the cycle. In contrast, moderate frequency ($\Omega = 0.085$) profiles combine characteristics of the low and high frequency cases. Surfinactant buildup in the transition region during retrograde flow can be seen in profiles (*e*) and (*f*). Unlike the high frequency case,

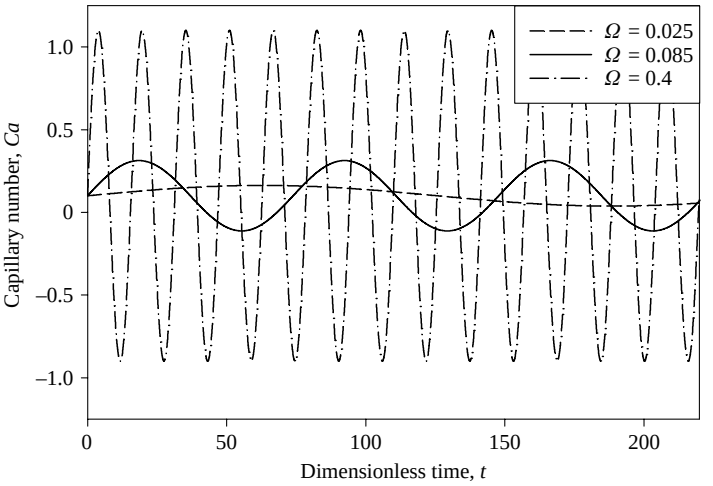

FIGURE 12. Capillary number *vs.* time for low ($\Omega = 0.025$), moderate ($\Omega = 0.085$), and high ($\Omega = 0.4$) frequencies for $Ca_M = 0.1$, $A = 5$. Note that the pulsatile amplitude increases with the dimensionless frequency as the period of oscillation increases.

though, this buildup is maintained in the bubble cap region during forward-phase portions of the cycle, as established by the tip concentration buildup seen in profiles (*a–d*). As will be demonstrated below, this response has implications regarding the cycle-averaged concentration response. Although not presented explicitly here, qualitatively similar low, moderate, and high frequency behaviour is seen for the multilayer model investigation of $Ca_M = 0.1$ and $A = 1$.

4.3. *Cycle-averaged concentrations*

To compare the overall system behaviour for a given Ca_M and A over a range of dimensionless frequencies, concentration averaging techniques are implemented. A cycle-averaged interfacial concentration profile is defined as

$$\bar{\Gamma}_i(s) \equiv \frac{1}{T}\int_{t_{conv}}^{t_{conv}+T} \Gamma_i(s,t)\,\mathrm{d}t, \tag{28}$$

where t_{conv} is a time reflecting system convergence to stationary state, and T is the oscillation period.

Figure 14 represents the monolayer model $\bar{\Gamma}$ for low, moderate, and high frequencies ($\Omega = 0.025$, 0.085, 0.4) for $Ca_M = 0.1$, $A = 5$. For $\Omega = 0.025$, $\bar{\Gamma}$ is characterized by significant buildup ($\bar{\Gamma} \sim 1.2$) at the bubble tip and depletion in the transition region. This profile resembles the concentration for steady forward motion. In contrast, at $\Omega = 0.4$ there is limited buildup of $\bar{\Gamma}$ in the bubble transition region ($\bar{\Gamma} \sim 0.6$ at $s \sim 0.3$), but an average surfinactant depletion ($\bar{\Gamma} \sim 0.3$) exists at the tip. Finally, the $\bar{\Gamma}$ profile for the moderate frequency ($\Omega = 0.085$) combines elements of both the high and the low frequency profiles – relatively high concentration ($\bar{\Gamma} \sim 0.9$) at the tip and significant concentration in the transition region ($\bar{\Gamma} \sim 0.55$ at $s \sim 0.5$). The elevation of $\bar{\Gamma}$ at the bubble tip during moderate oscillation translates to a larger concentration in the transition region at moderate s. Thus, the transport to the tip region has a potentially significant impact on the concentration in the thin film.

Figure 15 represents $\bar{\Gamma}_i$ of the multilayer model primary (*a*) and secondary (*b*) layers at low, moderate, and high frequencies ($\Omega = 0.025$, 0.085, 0.4) for $Ca_M = 0.1$, $A = 5$. At

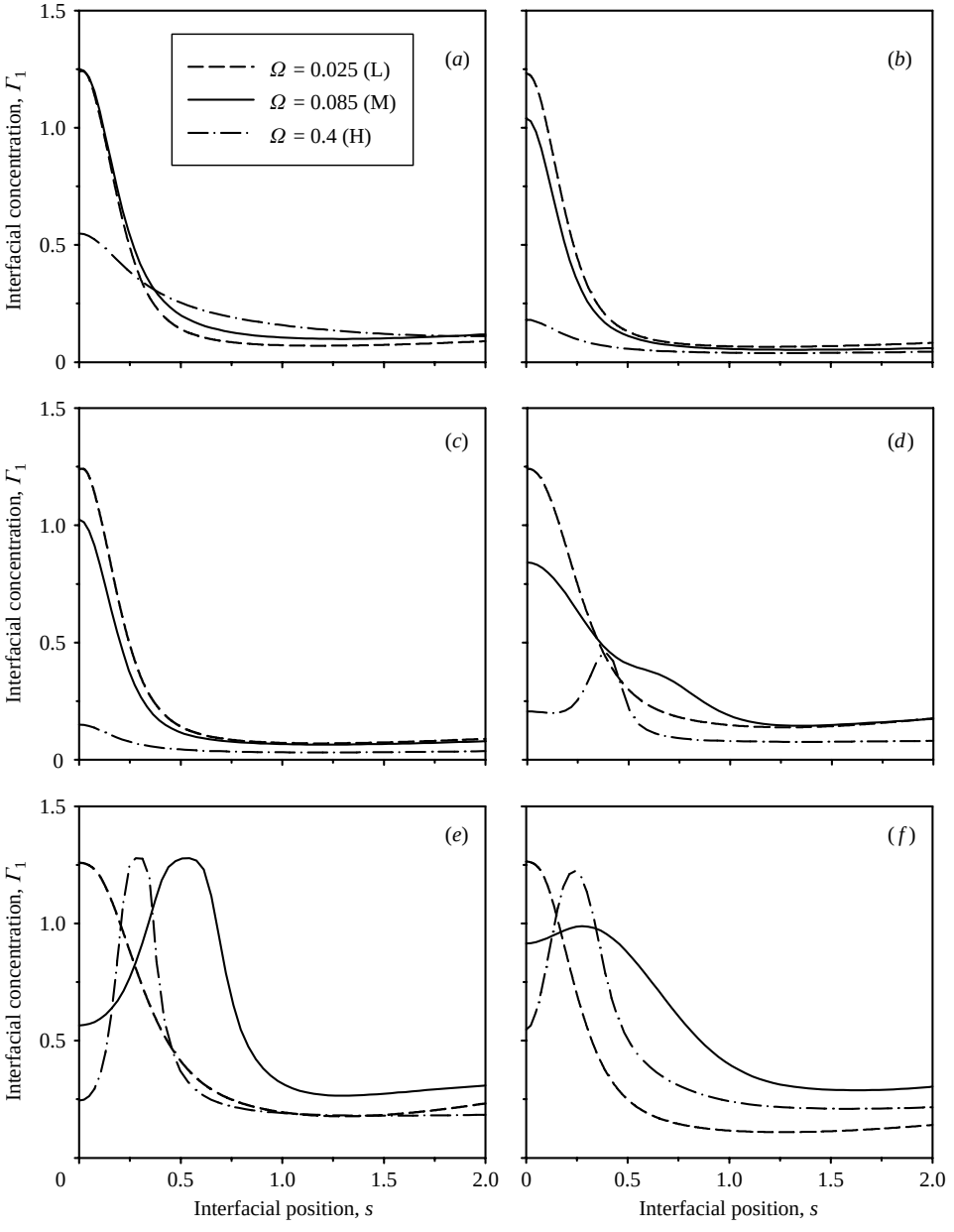

FIGURE 13. Monolayer-model interfacial surfinactant concentration (Γ_1) versus interfacial position (s) at evaluation points (a–f) spaced every 1/6th of the cycle for low ($\Omega = 0.025$), moderate ($\Omega = 0.085$), and high ($\Omega = 0.4$) frequencies for $Ca_M = 0.1$, $A = 5$.

low frequency ($\Omega = 0.025$), $\bar{\Gamma}_1$ is similar to the monolayer case, showing significant buildup ($\bar{\Gamma}_1 \sim 1.2$) at the bubble tip and depletion in the transition region. $\bar{\Gamma}_2$ for low frequency oscillation also shows significant buildup ($\bar{\Gamma}_2 \sim 1.8$) at the bubble tip; however for $s > 0.5$, there is an insignificant 2° layer present.

In contrast, at moderate frequency ($\Omega = 0.085$) a buildup of $\bar{\Gamma}_1$ in the bubble transition region exists ($\bar{\Gamma}_1 \sim 0.6$), and a high average surfinactant concentration ($\bar{\Gamma}_1 \sim 1.0$)

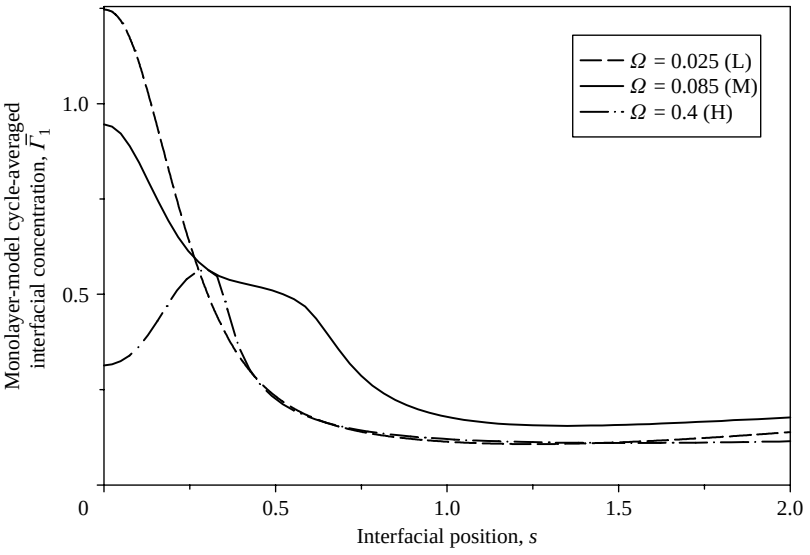

FIGURE 14. Monolayer-model cycle-averaged interfacial surfinactant concentration ($\bar{\Gamma}_1(s)$) versus interfacial position (s) for low ($\Omega = 0.025$), moderate ($\Omega = 0.085$), and high ($\Omega = 0.4$) frequencies for $Ca_M = 0.1$, $A = 5$.

resides at the tip. As with the monolayer model, this increase in surfinactant concentration translates to higher concentrations in the thin-film region. The $\bar{\Gamma}_2$ profile for moderate oscillation also shows limited surfinactant presence at the tip and in the transition region ($\bar{\Gamma}_2 \sim 0.25$).

At high frequency ($\Omega = 0.4$), there is a buildup of $\bar{\Gamma}_1$ in the bubble transition region ($\bar{\Gamma}_1 \sim 0.6$), but a lower average concentration ($\bar{\Gamma}_1 \sim 0.35$) exists at the tip. The $\bar{\Gamma}_2$ profile for high oscillation shows very low tip concentrations ($\bar{\Gamma}_2 \sim 0.1$) and limited transition-region buildup ($\bar{\Gamma}_2(s) \sim 0.3$).

4.4. *Cycle-spatial averaged concentrations*

In order to provide a quantitative comparison of the average amount of interfacial surfinactant in the bubble cap region for a given Ca_M and A combination, a spatial average of $\bar{\Gamma}_i(s)$ of each dimensionless frequency was taken over the domain $0 \leqslant s \leqslant \pi/2$. This cycle-spatial average is defined as

$$\langle \bar{\Gamma}_j \rangle \equiv \frac{1}{\pi/2} \int_{s=0}^{s=\pi/2} \bar{\Gamma}_i(s)\, \mathrm{d}s. \tag{29}$$

The range $0 \leqslant s \leqslant \pi/2$ was selected because it encompasses the entire cap region for a semicircular bubble. As such, all the dynamic recirculating activity near the bubble tip should be contained in this portion of the domain.

Figure 16 shows the monolayer-model cycle-spatial averaging of interfacial surfinactant concentration $\langle \bar{\Gamma}_1 \rangle$ versus dimensionless frequency over the range $0.05 < \Omega < 0.6$ for $Ca_M = 0.1$, $A = 5$. The reference value for $\langle \bar{\Gamma}_1 \rangle$ from steady-state $Ca_M = 0.1$ is also presented. At low frequencies, the system tends to behave similar to the system under steady-state forward motion conditions. As Ω is increased, $\langle \bar{\Gamma}_1 \rangle$ increases to a peak ($\langle \bar{\Gamma}_1 \rangle \sim 0.38$) near the moderate frequency ($\Omega \sim 0.085$) before quickly decreasing at higher frequencies. This behaviour will be explained in § 5.

Figure 17 shows the multilayer model cycle-spatial average of interfacial surfinactant concentration $\langle \bar{\Gamma}_i \rangle$ versus Ω over the range $0.05 < \Omega < 0.6$ for $Ca_M = 0.1$, $A = 5$.

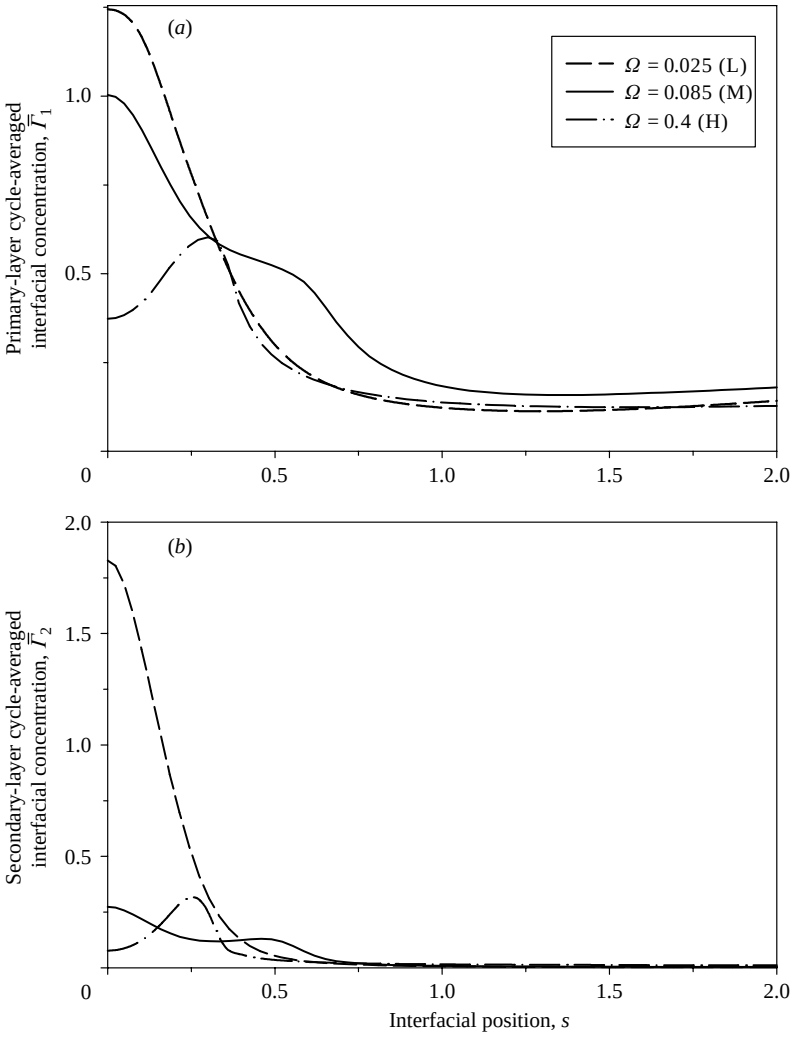

FIGURE 15. Multilayer-model cycle-averaged concentration of interfacial surfinactant ($\bar{\Gamma}_i(s)$) primary (*a*) and secondary (*b*) layers versus interfacial position s for low ($\Omega = 0.025$), moderate ($\Omega = 0.085$), and high, ($\Omega = 0.4$) frequencies for $Ca_M = 0.1$, $A = 5$.

The behaviour of $\langle \bar{\Gamma}_1 \rangle$ is similar to that discussed for the monolayer case; however, the concentrations for the multilayer model are greater than those of the monolayer model. For example, the moderate frequency ($\Omega \sim 0.085$) peak is slightly higher ($\langle \bar{\Gamma}_1 \rangle \sim 0.4$).

The 2° layer cycle–spatial average ($\langle \bar{\Gamma}_2 \rangle$) follows a different pattern from that of the 1° layer. With increasing Ω, $\langle \bar{\Gamma}_2 \rangle$ decreases to a minimum before the primary layer peak is reached ($\langle \bar{\Gamma}_2 \rangle \sim 0.05$ at $\Omega \sim 0.075$). As Ω is increased further, $\langle \bar{\Gamma}_2 \rangle$ rebounds slightly before again decreasing at higher Ω. The moderate frequency $\langle \bar{\Gamma}_2 \rangle$ does not recover to the $\langle \bar{\Gamma}_2 \rangle$ for steady flow before the high-frequency attenuation is seen. Despite this, the 2° layer is important because it increases the 1° layer cycle–spatial average concentration (figure 17) through respreading and inhibited desorption, as will be shown below.

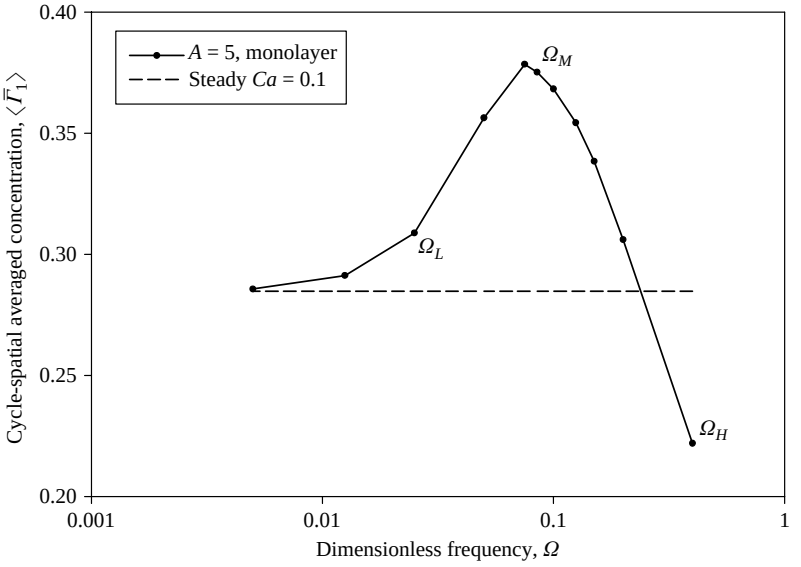

FIGURE 16. Monolayer-model cycle-spatial averaging of interfacial surfinactant concentration ($\langle \bar{\Gamma}_1 \rangle$) versus dimensionless frequency for $Ca_M = 0.1$, $A = 5$. The steady-state $Ca = 0.1$ monolayer-model interfacial surfinactant concentration spatial average ($s < \pi/2$) is shown for reference. $\Omega_L = 0.025$, $\Omega_M = 0.085$ and $\Omega_H = 0.4$.

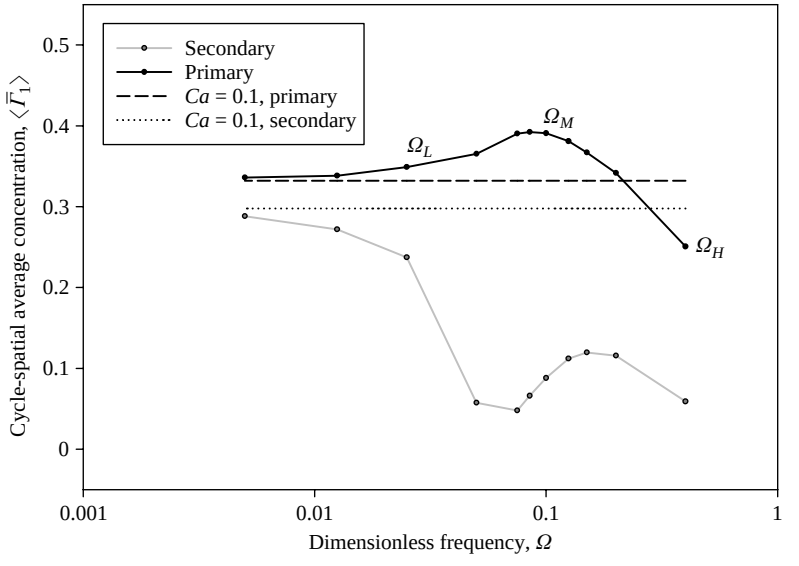

FIGURE 17. Multilayer-model cycle-spatial averaging of interfacial surfinactant concentration for primary (1°) and secondary (2°) layers ($\langle \bar{\Gamma}_i \rangle$) versus dimensionless frequency for $Ca_M = 0.1$, $A = 5$. The steady-state $Ca = 0.1$ multilayer-model interfacial surfinactant concentration spatial averages ($s < \pi/2$) for both primary and secondary layers are shown for reference. $\Omega_L = 0.025$, $\Omega_M = 0.085$ and $\Omega_H = 0.4$.

5. Discussion

We have shown above that oscillation superimposed on steady flow can modify the instantaneous flow field of a viscous fluid surrounding a semi-infinite bubble. This

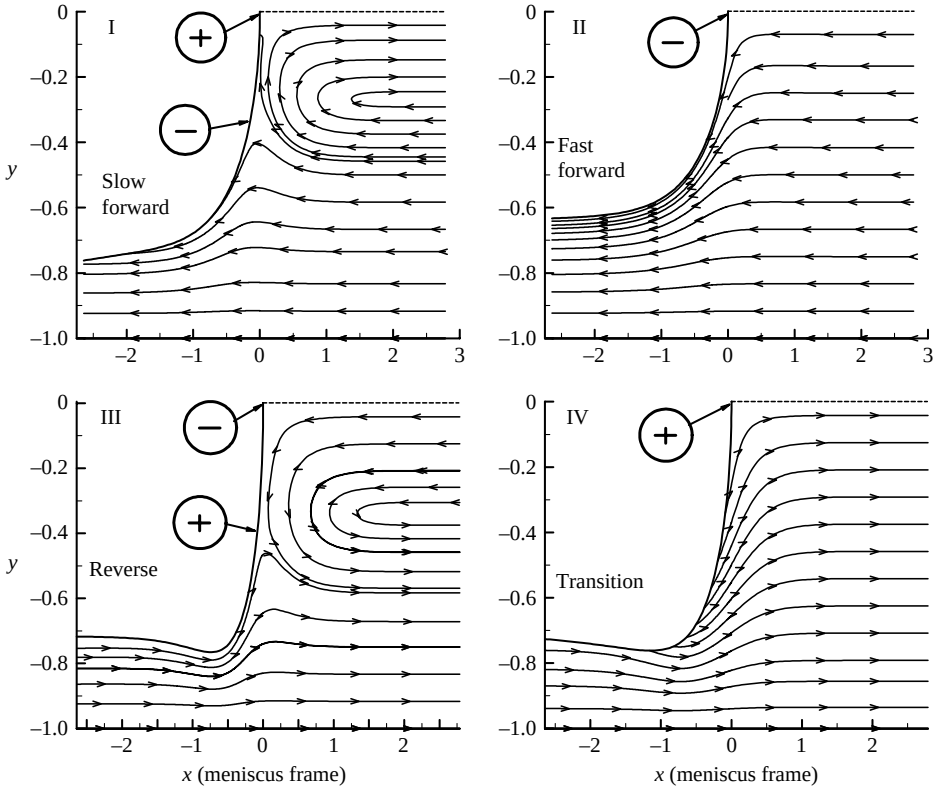

FIGURE 18. Streamline examples of the four main types of interfacial flow convergence: I, tip streamline convergence with a divergent transition-region stagnation point; II, tip streamline divergence only; III, tip streamline divergence with a convergent transition-region stagnation point; and IV, tip streamline convergence only.

results in an increase in the volume of liquid deposited onto the wall and modifies the average curvature of the bubble tip, which directly influences the transport of surfinactant to and from the bubble tip. In the previous section, we have shown that in the parameter ranges investigated, the interfacial surfinactant distribution during steady and pulsatile flow is non-equilibrium. buildup of surfinactant is directly coupled to the location of converging stagnation points along the interface. During pulsatile flow, a net increase of the average concentration in the bubble tip region over that seen in steady flow can be achieved through dynamic changes in the flow field. The goal of this section is to explain the interactions that result in surfinactant transport optimization.

5.1. *Flow field effects on surfinactant accumulation*

To explore the convective flow dynamics, we define four distinct cases of interfacial flow that can exist at any given time throughout a cycle of oscillation (figure 18 and table 5). The occurrence of each of these types of behaviour throughout a cycle of oscillation affects the buildup and retention of surfinactant in the bubble cap and transition regions.

Figure 19 shows the fraction of each cycle described by each flow type for $Ca_M = 0.1$ and $A = 5$. We characterize the dynamic flow field throughout one oscillation cycle over the range $0.025 \leqslant \Omega \leqslant 0.4$. At low frequencies ($\Omega \leqslant 0.04$), the interface behaves

Case	Flow condition	Tip stagnation	Transition region stagnation
I	Slow forward	Convergent	Divergent
II	Fast forward	Divergent	–
III	Reverse	Divergent	Convergent
IV	Transition	Convergent	–

TABLE 5. Characteristics of the four main types of interfacial flow.

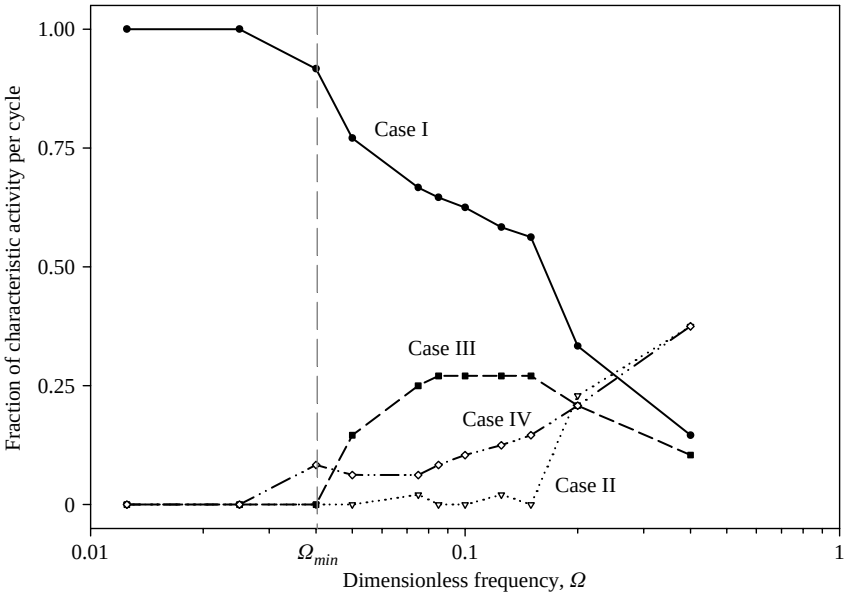

FIGURE 19. Interface flow characterization of dynamic interface throughout one oscillation cycle versus Ω for $Ca_M = 0.1$, $A = 5$. At any time, the interface can be classified into one of the four main groups described in figure 18 and table 5. The fraction of a cycle spent in each classification for a given frequency is presented.

as Case I throughout the cycle. With increasing Ω other categories of flow begin to occur during the oscillation. The interaction of surfinactant transport and this flow-field description can be used to explain the peak of $\langle \bar{\Gamma}_1 \rangle$ presented in figure 16.

For example, at low frequencies $\langle \bar{\Gamma}_1 \rangle$ is nearly equal to its value during steady-state forward flow. This response coincides with Case I flow behaviour, driving surfinactant to the bubble tip and depleting it from the transition and thin-film regions. As Ω increases, the relative proportion of Case I flow decreases, and the fraction of Case III flow increases. Case III flow occurs as the bubble retracts during portions of the cycle and is responsible for buildup of surfinactant in the transition region. At moderate frequencies ($\Omega \sim 0.085$), there is a sufficient balance between these two flow categories to accumulate surfinactant in the transition region during reverse flow and maintain it in the bubble tip region during forward flow. This balance is responsible for the increase and peak of the cycle–spatial interfacial concentration shown in figure 16. At higher frequency values ($\Omega \sim 0.4$) the relative proportions of both the Case I and Case III flows are diminished. While there remains a portion of the cycle during which surfinactant can be accumulated in the bubble transition region, the dominance of the uniformly divergent Case II flow prevents this buildup from being maintained in

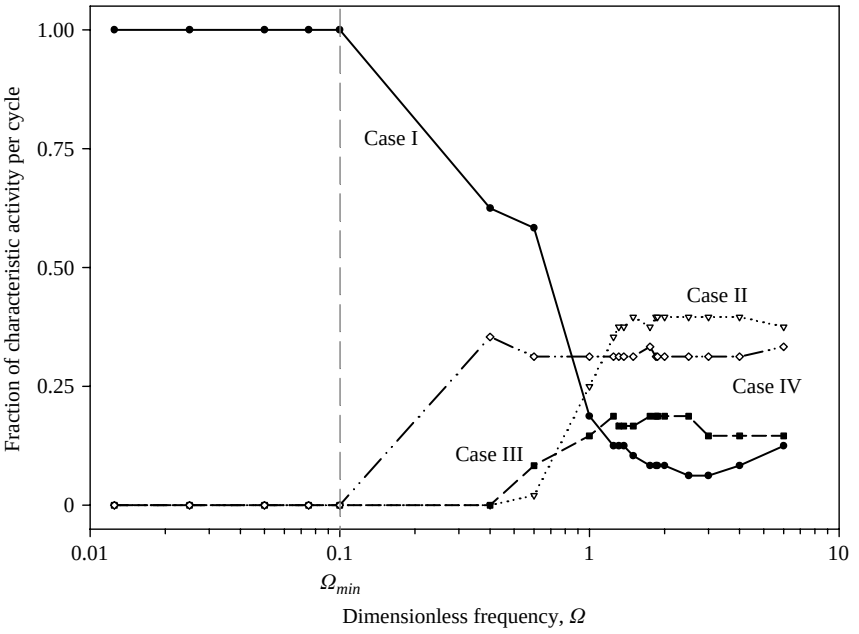

FIGURE 20. As figure 19 but for $A = 1$.

the interfacial region near the bubble tip throughout the cycle. This is reflected by the high-frequency attenuation of the cycle–spatial interfacial surfinactant concentration (figure 16).

Figure 20 shows the flow-field characterization with a reduction in amplitude ($Ca_M = 0.1$ and $A = 1$). The same general pattern of Case I–IV flows occurs over the range of Ω as for $A = 5$ (figure 19). Following the rationale described above, the peak transport should occur near $\Omega = 1$, since this frequency corresponds to the maximum fraction of Case III flow. Beyond this frequency, the Case I behaviour diminishes dramatically, and Case II (uniform divergence) depletes surfinactant from the interface.

The shift of the peak transport to higher Ω with a decrease in A is demonstrated in figure 21, which shows the relative behaviour of $\langle \bar{\Gamma}_1 \rangle$ over the range of frequencies for monolayer and multilayer simulations with $Ca_M = 0.1$ and $A = 1$ and 5. With multilayer simulations, respreading of the 2° layer during the tip flow divergence phase provides a localized surfinactant reservoir that maintains the 1° layer at a higher concentration as the frequency is elevated. At high frequencies, Case II flow without commensurate Case III behaviour causes a downturn in the multilayer average concentration profiles.

5.2. *General principles of surfinactant accumulation*

As demonstrated in the previous analysis, surfinactant accumulation in the transition region is insignificant unless retrograde flow exists during a portion of the cycle. For steady flow, this can only occur if $Ca < 0$. For unsteady flow, reverse flow will occur during a portion of the cycle if $Ca_\Omega > Ca_M$. Recalling that $Ca_\Omega = A\Omega/2$, the global onset of reverse flow will depend on stroke amplitude and frequency. We define $\Omega_{min} = 2(Ca_M/A)$ as the minimum frequency necessary to induce flow reversal. This relationship explains why an increase in A results in the decrease in Ω related to optimal sorption. Note, however, that the onset of Case III flow is not precisely aligned with Ω_{min} because the dynamic behaviour of the interface may allow forward

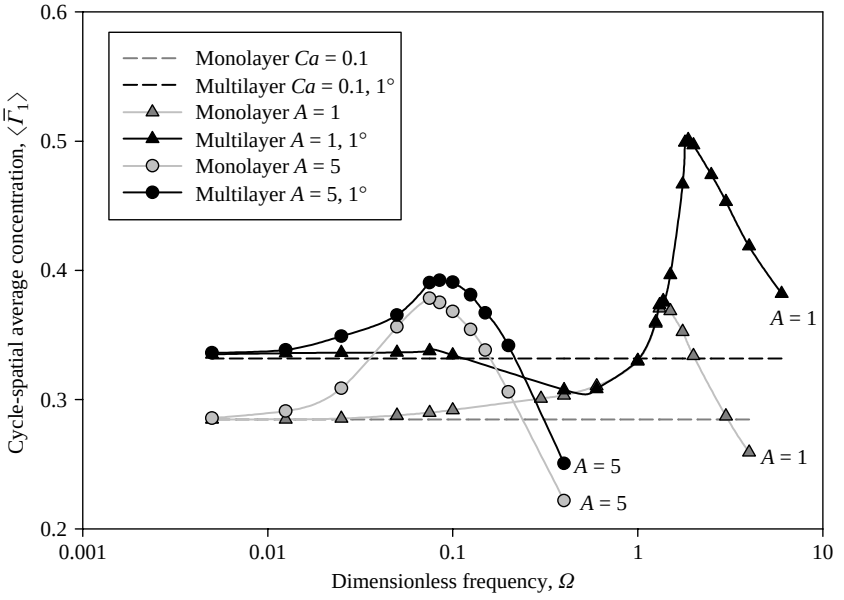

FIGURE 21. Cycle-spatial interfacial surfinactant concentration profiles versus Ω for monolayer and multilayer simulations with $Ca_M = 0.1$ and $A = 1, 5$.

flow to exist during parts of the cycle where $Ca(t) < 0$. This is particularly evident in figure 20, where $\Omega_{min} = 0.1$, but Case III behaviour is only observed for $\Omega > 0.4$. Nevertheless, the onset of retrograde motion is a key factor in the accumulation of surfinactant at the interface.

At frequencies less than Ω_{min}, a slight increase in the cycle-spatial interfacial concentration over that seen for the steady reopening can occur due to the fluid mechanical effects associated with the dynamic flow. For example, in the case of $\Omega = 0.025$ for $Ca_M = 0.1$ and $A = 5$ (figure 16), $\langle \bar{\Gamma}_1 \rangle$ is elevated with respect to the $Ca_M = 0.1$ case due to the dynamic change in position of the transition-region stagnation point. While this increase can occur for $\Omega < \Omega_{min}$, the induction of reverse flow when $\Omega > \Omega_{min}$ has a much more pronounced effect. At moderate frequencies, a balance of Case I and Case III flows allows for the local deposition of surfinactant in the transition region during retrograde flow portions of the cycle and retention of this buildup in the bubble cap region throughout forward flow portions of the cycle. This results in a peak in the cycle-spatial averaged concentration. Finally, at very high frequencies the large instantaneous Ca causes uniformly divergent Case II flow that sweeps surfinactant away from the cap region of the bubble. Any buildup created during a portion of the high-frequency cycle is irreversibly lost to the thin film. The dominance of Case III flow at elevated frequencies is responsible for the maximized peak accumulation seen at an optimal oscillation frequency Ω_{peak}.

Figure 21 shows that for multilayer simulations, inhibited desorption due to 2° layer formation elevates $\langle \bar{\Gamma}_1 \rangle$ with respect to corresponding monolayer data. The uniform interfacial flow divergence (Case II) at high frequencies allows respreading of the 2° layer, providing a localized surfinactant reservoir that maintains the 1° layer at a higher concentration for these elevated frequencies. This behaviour explains the reduction of $\langle \bar{\Gamma}_2 \rangle$ near Ω_{peak} as shown in figure 17. This results in a shift of Ω_{peak} to a higher frequency when multilayer dynamics are incorporated.

5.3. *Limitations*

As with all modelling studies, there are several limitations to the analyses presented herein. Primarily, these limitations include the absence of non-equilibrium surface tension and Marangoni stresses in the system, neglecting the effect of fluid inertia near the bubble tip, and the possibility of unsteady Stokes flow at high frequencies. In addition, the model does not take into account any mechanical characteristics of multilayer interfacial structures, nor does it allow for multiple multilayer formation.

If an equation of state relating interfacial tension to local surfactant concentration were incorporated into the model, the interfacial rigidification caused by the Marangoni stresses would modify surfactant convection along the meniscus. Ghadiali & Gaver (2003) showed that non-equilibrium surface tensions and Marangoni stresses can be very large and can modify flow fields and surfactant distributions from the constant surface tension case. The inclusion of Marangoni stress would allow surfactant deposited along the interface to convect to regions of lower concentrations. However, when concentrations become very large, the slope of the equation of state decreases. Thus, when Γ is large, the Marangoni stresses may lose their significance. Nevertheless, Marangoni stresses are likely to result in a modification of the frequency range of elevated transport for any given combination of Ca_M and A.

As described in § 2.2, we scaled-up Ca from 10^{-3} to 10^{-1} for numerical tractability. Although the values of St and Pe were commensurately modified to provide the correct transport balances, some of the properties of this system may still deviate from those of the physiological system. In particular, by increasing Ca, we observe Case II (uniformly divergent) flow during high-frequency oscillation. This flow field is responsible for the reduction of interfacial transport (§ 5.2). This type of flow would not be likely in the lung under constant surface tension conditions, because it is associated with very large Ca (i.e. $Ca(t) > 0.5$). However, with surface activity and a buildup of surfactant at the bubble tip, we expect that the forward phase may occur with very small tip surface tension. This could result in large $Ca = \mu Q/(2a\gamma)$ for even a moderate flow rate. Thus, under physiological conditions the Case II behaviour may continue to exist, albeit at lower velocities than those observed in the present study.

Our model has neglected inertial effects. Far from the bubble tip this assumption is acceptable because the Reynolds number based upon the convective velocity ($Re = \rho Q^*_{2-d}/2\mu$) is too small to induce significant effects. However, near the bubble tip the effects of inertia are governed by $Re/Ca = \rho\gamma a/\mu^2$. As Heil (2000, 2001) has demonstrated, these inertial effects can be significant for semi-infinite bubbles in rigid tubes or with flexible airways. It is important to recognize that our assumption might limit the validity of this analysis due to modification of convection patterns resulting from these inertial effects.

We have also neglected unsteady effects in our solution to the viscous flow field, though we included unsteadiness in the kinematic boundary condition. At high frequencies, it is possible that the assumption of Stokes flow is not valid. In general, to neglect unsteadiness the system Womersley number ($\alpha = a\sqrt{\omega/\nu}$), a measure of flow unsteadiness in the system, should be small. If $\alpha > 1$, the Stokes boundary layer will be small compared to the channel width, and could modify the flow field significantly near the interface. In addition, the inclusion of inertia in unsteady flows leads to phase differences between the pressure and flow fields. Future studies should thus investigate the effects of Stokes boundary layers and the impact of the pressure/flow phase lag on the behaviour of the system.

The model does not account for any structural characteristics of interfacial multilayers. The current model presumes that the multilayer only serves to alter the transport characteristics of the 1° interfacial layer. It is possible that the presence of multilayer structures tethered to the meniscus interface could alter the effect of the flow field on the bubble. If the multilayer model is not trilayer-limited (single 1° layer and double 2° layer), formation of multiple multilayers could allow for increased amounts of localized respreading and affect the mechanical characteristics of the surface structures.

6. Conclusions

In this paper, we have investigated the pulsatile motion of a semi-infinite bubble in a narrow channel and predicted the adsorption of inactive surface-active contaminant to the interface. This problem may be important for understanding film deposition processes. Our particular interests relate to surfactant deficiency in the lung. In the present study, a two-dimensional computational model of a pulsatile semi-infinite bubble delivery system was developed. It incorporates interfacial flow characteristics, multilayer transport dynamics, and flow-field characteristics of fluid surrounding the bubble tip using a coupled lubrication theory and boundary element method strategy. This model demonstrates that cyclic stretching and contraction of the penetrating interface could enhance surfactant deposition and retention in the bubble cap region, thereby increasing the penetration depth of surfactant delivery and minimizing potential lung injury from high ventilation pressures.

Computational analysis of the system at a fixed Ca_M and A identified a range of frequencies of oscillation that may increase the transport of a passive surface-associated contaminant (surfinactant). While the dynamic interfacial modification seen at low frequencies can lead to limited surfinactant accumulation in the bubble cap region (Case I), a minimum critical frequency Ω_{min} must be achieved in order to induce retrograde flow during portions of the pulsatile cycle. Creation of retrograde flow allows for the focused deposition of surfinactant away from the bubble tip in the interfacial transition region. This retrograde deposition is retained in the bubble cap region at moderate frequencies (Case III), but it is lost to the thin-film region at high frequencies as a result of uniform interfacial flow divergence due to rapid forward motion during the cycle (Case II). Before this divergence occurs, an optimal frequency (Ω_{peak}) exists that maximizes surfinactant retention in the bubble cap region.

It can be noted that decreasing A shifts Ω_{peak} to higher frequencies (figure 21). While this may be seen as an advantage for the larger A case, the maximum cycle-spatial average of surfinactant is significantly higher for the lower amplitude system. For a given Ca_M, we hypothesize that a specific A could be identified that produces a minimized optimal frequency while maintaining sufficient peak concentrations. Extending this theory to physiologic models suggests that a combination of low oscillation frequency and high interfacial surfactant concentrations might lead to minimized lung epithelial damage and maximized effectiveness of surfactant replacement therapy. However, it is necessary to improve our models to account for physiochemical effects and fluid–structure interactions prior to making specific estimates of optimal ventilation frequencies and amplitudes.

The authors would like to thank Professor David Halpern, Bryan Smith and Anne-Marie Jacob for their help with this work. This work was supported by

the National Science Foundation (BES-9978605) and NASA (NAG3-2734), and the National Institutes of Health (1 P20 EB001432-01).

REFERENCES

Bilek A. M., Dee, K. C., & Gaver III, D. P. 2003 Mechanisms of surface-tension-induced epithelial cell damage in a model of pulmonary airway reopening. *J. Appl. Physiol.* **94**, 770–783.

Bretherton, F. P. 1961 The motion of long bubbles in tubes. *J. Fluid Mech.* **10**, 166–188.

Diamant, H., Witten, T. A., Gopal, A., & Lee, K. Y. C. 2000 Unstable topography of biphasic surfactant monolayers. *Europhys. Lett.* **52**, 171–177.

Ding, J., Takamoto, D. Y., von Nahmen, A., Lipp, M. M., Lee, K. Y., *et al.* 2001 Effects of lung surfactant proteins, SP-B and SP-C, and palmitic acid on monolayer stability. *Biophys J.* **80**, 2262–2272.

Dos Santos, C. C., & Slutsky, A. S. 2000 Invited review: mechanisms of ventilator-induced lung injury: a perspective. *J. Appl. Physiol.* **89**, 1645–1655.

Eckmann, D. M. & Diamond, S. L. 2004 Surfactants attenuate gas embolism-induced thrombin production. *Anesthesiology* **100**, 77–84.

Fairbrother, F. & Stubbs, A. E. 1935 Studies in electroendosmosis. Part IV. The bubble-tube method of measurement. *J. Chem. Soci.* **1**, 527–529.

Fujiwara, T., Maeta, H., Chida, S., Morita. T., Watabe, Y. & Abe, T. 1980 Artificial surfactant therapy in hyaline-membrane disease. *Lancet* **1**, 55–59.

Gaver III, D. P., Halpern, D., Jensen, O. E. & Grotberg, J. B. 1996 The steady motion of a semi-infinite bubble through a flexible-walled channel. *J. Fluid Mech.* **319**, 25–65.

Gaver III, D. P., Samsel, R. W. & Solway, J. 1990 Effects of surface tension and viscosity on airway reopening. *J. Appl. Physiol.* **69**, 74–85.

Geng, X., Yuan, H., Oguz, H. N. & Prosperetti, A. 2001 Bubble-based micropump for electrically conducting liquids. *J. Micromech. Microengng* **11**, 270–276.

Ghadiali, S. N., Banks, J. & Swarts J. D. 2002 Effect of surface tension and surfactant administration on Eustachian tube mechanics. *J. Appl. Physiol.* **93**, 1007–1014.

Ghadiali, S. N. & Gaver III, D. P. 2000 An investigation of pulmonary surfactant physicochemical behavior under airway reopening conditions. *J. Appl. Physiol.* **88**, 493–506.

Ghadiali, S. N. & Gaver III, D. P. 2003 The influence of non-equilibrium surfactant dynamics on the flow of a semi-infinite bubble in a rigid cylindrical capillary tube. *J. Fluid Mech.* **478**, 165–196.

Grotberg, J. B. 2001 Respiratory fluid mechanics and transport processes. *Annu. Rev. Biomed. Engng* **3**, 421–457.

Halpern, D. & Gaver III, D. P. 1994 Boundary-element analysis of the time-dependent motion of a semi-infinite bubble in a channel. *J. Comput. Phys.* **115**, 366–375.

Halpern, D., Jensen, O. E. & Grotberg, J. B. 1998 A theoretical study of surfactant and liquid delivery into the lung. *J. Appl. Physiol.* **85**, 333–352.

Hazel, A. L. & Heil, M. 2003 Three-dimensional airway reopening: the steady propagation of a semi-infinite bubble into a buckled elastic tube. *J. Fluid Mech.* **478**, 47–70.

Heil, M. 2000 Finite Reynolds number effects in the propagation of an air finger into a liquid-filled flexible-walled channel. *J. Fluid Mech.* **424**, 21–44.

Heil, M. 2001 Finite Reynolds number effects in the Bretherton problem. *Phys. Fluids* **13**, 2517–2521.

Jensen, O. E., Horsburgh, M. K., Halpern, D. & Gaver III, D. P. 2002 The steady propagation of a bubble in a flexible-walled channel: Asymptotic and computational models. *Phys. Fluids* **14**, 443–457.

Kay, S. S., Bilek, A. M., Dee, K. C. & Gaver III, D. P. 2004 Pressure gradient, not exposure duration, determines the extent of epithelial cell damage in a model of pulmonary airway reopening. *J. Appl. Physiol.*

Krishnan, J. A. & Brower, R. G. 2000 High-frequency ventilation for acute lung injury and ARDS. *Chest* **118**, 795–807.

Krueger, M. A. & Gaver III, D. P. 2000 A theoretical model of pulmonary surfactant multilayer collapse under oscillating area conditions. *J. Colloid Interface Sci.* **229**, 353–364.

Lipp, M. M., Lee, K. Y. C., Takamoto, D. Y., Zasadzinski, J. A. & Waring A. J. 1998 Coexistence of buckled and flat monolayers. *Phys. Rev. Lett.* **81**, 1650–1653.

Lu, W., Knobler, C. M., Bruinsma, R. F., Twardos, M. & Dennin, M. 2002 Folding langmuir monolayers. *Phys. Rev. Lett.* **89**, 146107.

MacDorman, M. F., Minino, A. M., Strobino, D. M. & Guyer, B. 2002 Annual summary of vital statistics – 2001. *Pediatrics* **110**, 1037–1052.

Pozrikidis, C. 1992 *Boundary Integral and Singularity Methods for Linearized Viscous Flow*. Cambridge University Press.

Ratulowski, J. & Chang, H. C. 1990 Marangoni effects of trace impurities on the motion of long gas-bubbles in capillaries. *J. Fluid Mech.* **210**, 303–328.

Stone, H. A. 1990 A simple derivation of the time-dependent convective-diffusion equation for surfactant transport along a deforming interface. *Phys. Fluids.* A **2**, 111–112.

Takamoto, D. Y., Lipp, M. M., von Nahmen, A., Lee, K. Y., Waring, A. J. & Zasadzinski, J. A. 2001 Interaction of lung surfactant proteins with anionic phospholipids. *Biophys. J.* **81**, 153–169.

Taylor, G. I. 1961 Deposition of a viscous fluid on the wall of a tube. *J. Fluid Mech.* **10**, 161–165.

Whitehead, T. & Slutsky, A. S. 2002 The pulmonary physician in critical care – **7**: Ventilator induced lung injury. *Thorax* **57**, 635–642.

Yap, D. Y. K. & Gaver III, D. P. 1998 The influence of surfactant on two-phase flow in a flexible-walled channel under bulk equilibrium conditions. *Phys. Fluids* **10**, 1846–1863.

Yap, D. Y. K., Liebkemann, W. D., Solway, J. & Gaver III, D. P. 1994 Influences of parenchymal tethering on the reopening of closed pulmonary airways. *J. Appl. Physiol.* **76**, 2095–2105.